

IMPERIAL COLLEGE LONDON

DEPARTMENT OF ELECTRICAL AND ELECTRONIC ENGINEERING

Signal Optimization for Wireless Information and Power Transmission

Student:
Yang Zhao

Supervisor:
Dr Bruno Clerckx

Co-Supervisor:
Dr Morteza Varasteh

A thesis submitted for the degree of
MSc Communications and Signal Processing

September 5, 2019

Abstract

Wireless can be more than communications. As a medium of information and energy, the radio wave enables a unified Wireless Information and Power Transfer (WIPT) to link and charge low-power devices remotely. This paper departs from the rectifier behavior to derive a nonlinear energy harvester model and investigate the relationship between waveform design and power transmission. On top of that, a superposition of multi-carrier modulated and unmodulated multisine waveforms is introduced to improve the rate-energy (R-E) tradeoff. With an adaptive transceiver design, we jointly optimize the superposed signal at the transmitter and the power splitter at the receiver according to the channel state information. We then extend the existing works to MIMO and consider the influence of frequency selectivity and PAPR constraints. Based on non-convex posynomial maximization, the iterative algorithms are demonstrated to enlarge the R-E region for multi-carrier transmissions. Numerical results also highlight the importance of modeling harvester nonlinearity in WIPT system design.

Contents

1	Introduction	5
1.1	Background	5
1.2	Literature Review	5
1.3	Objectives and Methodology	6
2	From WPT to WIPT	7
2.1	WPT Architecture	7
2.2	Rectenna Design	8
2.2.1	Rectifier Behavior	8
2.2.2	Antenna Model	9
2.2.3	Diode Characteristics	10
2.3	Receiver Architectures	12
2.3.1	Time Switching	12
2.3.2	Power Splitting	12
2.4	Signal and System Model	12
2.4.1	Transmitted Information Waveform	13
2.4.2	Transmitted Power Waveform	14
2.4.3	Channel and Received Waveform	15
2.4.4	Information Decoder	15
2.4.5	Energy Harvester	16
3	Rate-Energy Tradeoff	19
3.1	Rate-Energy Region	19
3.2	Problem Formulation	19
3.3	Iterative Algorithms	21
3.3.1	General Approach	21
3.3.2	Decoupled Design	22
3.3.3	Lower Bound	24
3.3.4	PAPR Constraints	25
3.3.5	Multiple Rectennas	27
4	Performance Evaluation	31
4.1	SISO	31
4.1.1	R-E Region vs Subband	32
4.1.2	R-E Region vs SNR	34
4.1.3	R-E Region vs PAPR	36
4.2	MISO	38
4.3	MIMO	39

5	Conclusions and Future Works	41
A	Appendix	42

List of Figures

2.1	Block diagram of a generic far-field WPT system [1]	7
2.2	A typical 3-subcarrier multisine and single sine [2]	9
2.3	Rectenna architecture [3]	9
2.4	Structure of TS receiver [4]	12
2.5	Structure of PS receiver [4]	13
4.1	Frequency response of the SISO FF and FS channels	32
4.2	R-E region vs N for FF and FS channels	33
4.3	Optimal R-E region for FF channel with medium N	34
4.4	R-E region vs SNR for FF channel	35
4.5	R-E region vs SNR for FS channel	36
4.6	R-E region vs PAPR for FF channel	37
4.7	Frequency response of the MISO FF channels	38
4.8	R-E region vs M and N over typical FF channels	38
4.9	Rate and current CDF vs M for MISO FF channels	39
4.10	Frequency response of the MIMO FF channel	40
4.11	R-E region vs N and U for MIMO FF channels	40

List of Tables

4.1	Reference parameters used in the simulation	31
-----	---	----

Chapter 1

Introduction

1.1 Background

Energy-constrained wireless devices are conventionally powered by batteries. However, the development of large-scale networks as Internet-of-Things (IoT) is restricted by its limited working time and frequent recharging or replacement. Although Wireless Power Transfer (WPT) via inductive coupling has enjoyed some success in real-world applications, it is impractical for most devices on the move since the operation range is relatively short. As a promising alternative, the Radio-Frequency (RF) wave is with lower power level (μW to W) but broader coverage (up to hundreds of meters) [5]. Interestingly, it indeed carries both information and energy simultaneously, with the potential to power billions of mobile nodes wirelessly while keeping them connected. The recent revolution in harvester model and the significant drop of power requirement in electronics will bring more opportunities to the research on Wireless Information and Power Transfer (WIPT) via RF signals.

1.2 Literature Review

Significant achievements in WIPT has been witnessed in the last decade. The idea was first proposed in [6], where the author defined a concave capacity-energy function and investigated the tradeoff for typical binary channels and a flat additive white Gaussian noise (AWGN) channel with amplitude-constrained inputs. The research was extended to frequency-selective channel in [7]. However, both works were based on the impractical assumption that information decoding (ID) and Energy Harvesting (EH) can be performed individually on the same received signal. In [8], the authors proposed two practical co-located receiver designs named *time switching* (TS) that switches between ID and EH and *power splitting* (PS) that splits the received power into two separate streams. It was then demonstrated in [9] that TS can guarantee the same rate as conventional Time-Division Multiple Access (TDMA) while providing considerable power to the system. In comparison, PS may produce a higher rate when the power demand is sufficiently high. A further research [10] proposed a suboptimal low-complexity *antenna switching* scheme and enabled dynamic power splitting to adjust the split ratio with the channel state information (CSI). Nevertheless, the literature above relies on an oversimplified linear harvester model. To accurately characterize the behavior of the rectenna, [3] derived a tractable nonlinear model and performed an adaptive multisine waveform

design for WPT. Realistic simulations showed significant gains in harvested power and stressed the importance of modeling rectifier nonlinearity in wireless system design. The work was extended to multi-input single-output (MISO) WIPT in [11], where the multisine is superposed to a modulated information waveform and optimized adaptively to CSI. It suggested the rectifier nonlinearity can lead to a larger rate-energy (R-E) region, which favors a different waveform, modulation, and input distribution. In another perspective, a learning approach [12] modeled the transmitter and receiver as deep neural network (NN) and jointly optimized signal encoding with network parameters. Constellations showed that the offset of the power symbol is positively correlated to the power demand, while the information symbols are symmetrically located around the origin. The pattern confirmed that an unmodulated waveform is beneficial to increase the harvested power.

1.3 Objectives and Methodology

In this article, we depart from the rectifier behavior and diode characteristics to revisit the analytical harvester models proposed in [3]. On top of this, a multi-carrier modulated waveform and a multi-carrier unmodulated waveform are compared in terms of harvested energy. The results demonstrated that when considering rectifier nonlinearity, the unmodulated waveform outperforms the modulated waveform for multi-carrier WPT but is outperformed for single-carrier transmission. It is in sharp contrast to the conventional opinion based on linear rectifier model.

We also explore the adaptive transceiver design in [11] that jointly optimizes the superposed signal (consists of modulated and unmodulated components) at the transmitter and the power splitter at the receiver. The characterization of the R-E region is converted into an optimization problem that maximizes the harvested current under discrete rate constraints via Geometric Programming (GP) tools. The original strategy for Multiple-Input Single-Output (MISO) is extended to Multiple-Input Multiple-Output (MIMO) WIPT, and the Peak-to-Average Power Ratio (PAPR) constraint is introduced to the system. We then investigate the influence of frequency selectivity on R-E tradeoff.

Chapter 2

From WPT to WIPT

In this section, we first introduce a general WPT architecture. Next, we focus on the rectenna behavior and derive the analytical diode models for the energy harvester. We then extend the work to WIPT and explore two practical receiver structures. Finally, the signal and system model is established, and the dependency of delivered power on signal design is investigated on top of it.

2.1 WPT Architecture

According to the operation principle, WPT systems can be categorized as *maximum power transfer* that maximizes the coverage and *maximum energy efficiency transfer* that compromise with the power budget [13]. Fig. 2.1 illustrates the fundamental blocks of a generic far-field WPT system.

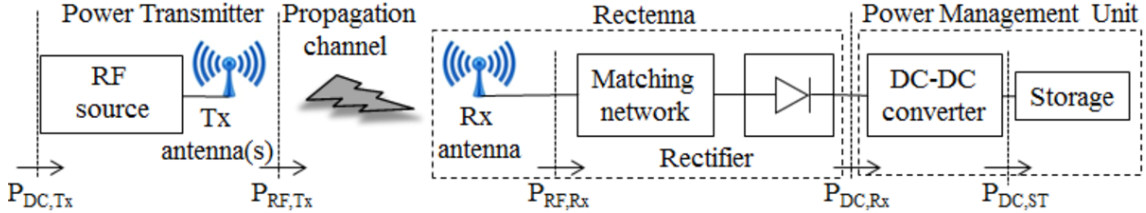


Figure 2.1: Block diagram of a generic far-field WPT system [1]

The transmit power efficiency e is decomposed as

$$e = \frac{P_{dc,ST}}{P_{dc}^t} = \underbrace{\frac{P_{rf}^t}{P_{dc}^t}}_{e_1} \cdot \underbrace{\frac{P_{rf}^r}{P_{rf}^t}}_{e_2} \cdot \underbrace{\frac{P_{dc}^r}{P_{rf}^r}}_{e_3} \cdot \underbrace{\frac{P_{dc,ST}}{P_{dc}^r}}_{e_4} \quad (2.1)$$

Most existing solutions assumed no dependency among the components and focused on maximizing each term individually. Nevertheless, it has been proved by [14, 3, 15] that these efficiencies are indeed coupled with each other, especially when input power is not very high (below 1 mW). Specifically, the DC-to-RF efficiency e_1 is related to signal PAPR and waveform design [16]. Similarly, the RF-to-RF efficiency e_2 is determined by the channel state and the signal characteristics as waveform, beamformer, modulation, and power allocation [4]. It also desires a highly directional transmission [17]. e_3 measures the RF-to-DC efficiency of the rectenna, which is a function of input power P_{rf}^r [2, 18, 1], channel state [3, 11], and

the waveform design [19, 20, 4]. The DC-to-DC efficiency e_4 can be improved by dynamically adjusting the load of the rectifier according to the diode impedance [21].

Therefore, waveform design plays an essential role in WPT systems by contributing to e_1, e_2, e_3 simultaneously. To maximize the overall power efficiency e , we establish an tractable relationship between the transmitted signal and the harvester output current in the following section.

2.2 Rectenna Design

2.2.1 Rectifier Behavior

A rectenna receives electromagnetic power via antenna and convert it to electric power with rectifier. Diverse configurations are available for energy harvesting, such as *Schottky* [22, 23], *CMOS* [24, 25], *series* [26, 27], *shunt* [28, 29]. It is worth noting that those models favor different input power levels. As reported in [25, 30], low barrier Schottky diodes are commonly used for input power between 1 μ W and 1 mW. Specifically, single diode is preferred for a power below 500 μ W while multiple diodes are more suitable for power above 500 μ W [4]. Hybrid designs as [31] may be employed to maintain a high efficiency for a wide power range.

Besides the rectenna model, the shape of the received signal also influences the RF-to-DC efficiency e_3 . It was first demonstrated in [2] that multisine waveform i.e. *Power-Optimized waveform* (POW) outperforms the single-tone waveform i.e. *Continuous Wave* (CW) in both operation range and power efficiency. Therefore, multisine is commonly employed in WPT waveform design.

The expression of a multisine waveform with N subcarriers writes as a summation of N sine waves

$$V_{\text{multisine}}(t) = \sum_{n=0}^{N-1} \frac{1}{\sqrt{N}} \sin(2\pi(f_0 + n\Delta f)t) \quad (2.2)$$

where f_0 is the minimum frequency and Δf is the spacing. Fig. 2.2 [2] illustrates a three-subcarrier multisine and single sine in time and frequency domains. It can be observed that multisine provides a higher PAPR of \sqrt{N} and occupies a bandwidth of $(N-1)\Delta f$. Compared with the single sine, it has the same average power but equally distributed to the components. The thick lines indicate typical rectifier output voltage.

The advantage of multisine is that high PAPR can be exploited to increase the peak output voltage of the rectifier. With a proper signal and circuit design, the high output voltage may be preserved during the cycle if discharging is slow enough (as indicated by the thick blue line in Fig. 2.2(b)). To enhance the harvested power, a large number of tones may be used to increase PAPR, and the multisine signal will appear as pulses with a period of $1/\Delta f$. Most of the signal power will be concentrated in those pulses to trigger the diode and charge the capacitor. However, more subbands can lead to smaller frequency gaps and longer charging cycle when the bandwidth is fixed.

It can be hard to derive an accurate expression of the RF-to-DC efficiency e_3 on the power and shape of the rectifier input signal, as practical energy harvesting

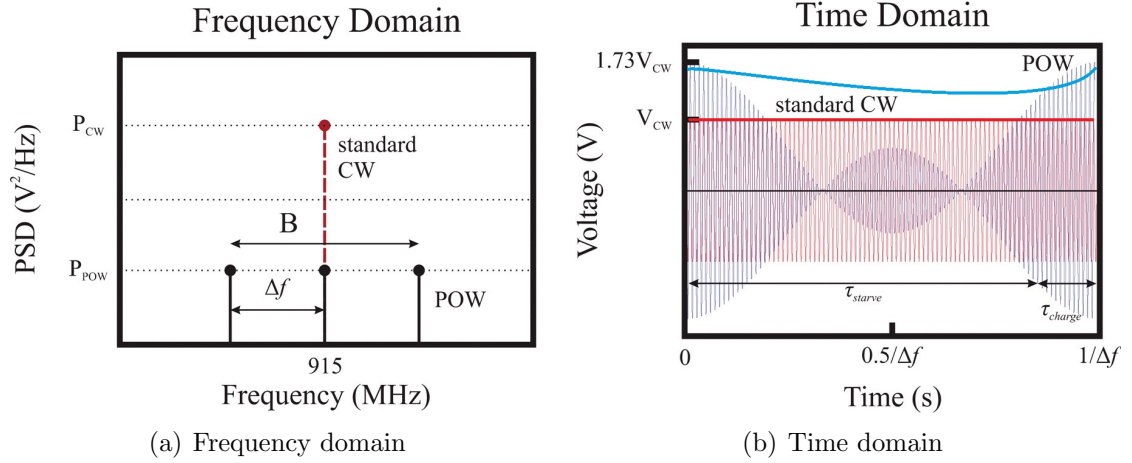


Figure 2.2: A typical 3-subcarrier multisine and single sine [2]

circuits consists of various nonlinear components like diodes, capacitors, and inductors. It is also sensitive to parasitic sources, impedance matching, and harmonic generation [32, 25]. In this article, we employ the *diode linear model* and *diode non-linear model* proposed in [3] based on the diode current-voltage (I-V) characteristics to capture the fundamental pattern of the rectifier and investigate its impact on resource allocation and system design. A superposed waveform containing modulated information and multisine power components is optimized according to CSI on top of both models.

2.2.2 Antenna Model

As illustrated in Fig. 2.3(a) [3], the rectifier consists of a single diode as the source of nonlinearity and a low-pass filter to store energy.

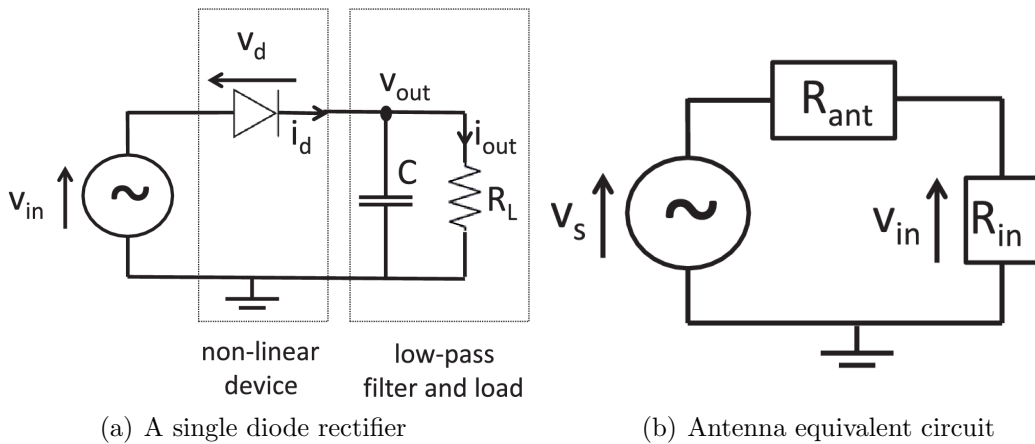


Figure 2.3: Rectenna architecture [3]

Fig. 2.3(b) illustrates the antenna equivalent circuit. It includes a voltage source $v_s(t)$ connected to a series antenna impedance $Z_{\text{ant}} = R_{\text{ant}} + jX_{\text{ant}}$, followed by a combined impedance of the rectifier and the matching network $Z_{\text{in}} = R_{\text{in}} + jX_{\text{in}}$. Assuming lossless, the perfect matching condition is

$$R_{\text{in}} = R_{\text{ant}}, X_{\text{in}} = -X_{\text{ant}} \quad (2.3)$$

When (2.3) is satisfied, the rectifier input voltage equals

$$v_{\text{in}}(t) = v_s(t)/2 = y(t)\sqrt{R_{\text{in}}} \quad (2.4)$$

where $y(t)$ is the received signal. Therefore, the input power to the rectifier is

$$P_{\text{rf}}^r = \mathbb{E}[y(t)^2] = \mathbb{E}[v_{\text{in}}(t)^2] / R_{\text{in}} \quad (2.5)$$

It is also assumed that the noise is too small to be harvested.

2.2.3 Diode Characteristics

Consider the single diode rectifier presented in Fig. 2.3(a) for simplicity. Without loss of generality, the diode models can be employed for other circuits as voltage doubler and bridge rectifiers [33].

Denoting $v_{\text{in}}(t)$ and $v_{\text{out}}(t)$ as diode input and output voltages, the voltage across the diode is $v_d(t) = v_{\text{in}}(t) - v_{\text{out}}(t)$. It determines the current flowing through the diode

$$i_d(t) = i_s \left(e^{\frac{v_d(t)}{nv_t}} - 1 \right) \quad (2.6)$$

where i_s is the reverse saturation current, n is the ideality factor, and v_t is the thermal voltage. With Taylor expansion around a quiescent point $a = v_d(t)$, (2.6) rewrites as

$$i_d(t) = \sum_{i=0}^{\infty} k'_i (v_d(t) - a)^i \quad (2.7)$$

with

$$k'_i = \begin{cases} i_s \left(e^{\frac{a}{nv_t}} - 1 \right), & i = 0 \\ i_s \frac{e^{\frac{a}{nv_t}}}{i!(nv_t)^i}, & i \in \mathbb{N}^+ \end{cases} \quad (2.8)$$

k'_i depends on the diode parameters and is a constant when a is fixed. Note that the Taylor series expression is a small-signal model that only fits the nonlinear operation region of the diode. Therefore, (2.7) is no longer accurate for a large input voltage $v_{\text{in}}(t)$, where the diode behavior is dominated by the series resistor and the I-V relationship is linear [23].

Also, we assume an ideal rectifier with steady-state response to deliver a constant output voltage v_{out} , whose amplitude is a function of the peaks of the input voltage $v_{\text{in}}(t)$ [34]. Based on those assumptions, a proper choice of voltage drop would be

$$a = \mathbb{E}[v_d(t)] = \mathbb{E}[v_{\text{in}}(t) - v_{\text{out}}] = -v_{\text{out}} \quad (2.9)$$

On top of (2.9) and (2.4), the diode current (2.7) can be further expressed as

$$i_d(t) = \sum_{i=0}^{\infty} k'_i v_{\text{in}}(t)^i = \sum_{i=0}^{\infty} k'_i R_{\text{ant}}^{i/2} y(t)^i \quad (2.10)$$

It reveals an explicit relationship between the received waveform $y(t)$ and the diode current $i_d(t)$. Nevertheless, the waveform varies at every symbol period due to the randomness of the input distribution. Hence, the diode current $i_d(t)$ also fluctuates with time. By taking an expectation over the symbol distribution, the harvested DC current can be modeled as

$$i_{\text{out}} = \mathbb{E}[i_d(t)] \quad (2.11)$$

so the available power is

$$P_{\text{dc}}^r = i_{\text{out}}^2 R_L = \mathbb{E}[i_d(t)]^2 R_L \quad (2.12)$$

To investigate the fundamental dependency of harvested power on waveform design, a practical strategy is to approximate (2.10) with truncation to the n_o -th order

$$i_{\text{out}} \approx \sum_{i=0}^{n_o} k'_i R_{\text{ant}}^{i/2} \mathbb{E}[y(t)^i] \quad (2.13)$$

The contribution of odd terms is indeed zero as $\mathbb{E}[y(t)^i] = 0$ for odd i . Therefore, the approximated rectifier output DC current equals

$$i_{\text{out}} \approx \sum_{i \text{ even}, i \geq 0}^{n_o} k'_i (i_{\text{out}}) R_{\text{ant}}^{i/2} \mathbb{E}[y(t)^i] \quad (2.14)$$

Recall from (2.8) that the diode parameter k'_i is a function of $a = -v_{\text{out}} = -i_{\text{out}} R_L$. Therefore, i_{out} occur in both sides of (2.14). [3] suggested an approach to decouple the correlation. Denote

$$k''_0 = e^{\frac{a}{nv_t}} = e^{-\frac{R_L i_{\text{out}}}{nv_t}} \quad (2.15)$$

such that $k'_0 = i_s(k''_0 - 1)$ and (2.14) rewrites as

$$e^{\frac{R_L i_{\text{out}}}{nv_t}} (i_{\text{out}} + i_s) \approx i_s + \sum_{i \text{ even}, i \geq 2}^{n_o} \frac{k'_i}{k''_0} R_{\text{ant}}^{i/2} \mathbb{E}[y(t)^i] \quad (2.16)$$

Note the r.h.s. of (2.16) is independent of i_{out} . On the other hand, the l.h.s. is a monotonic increasing function of i_{out} . Therefore, we can further write

$$k_i = \frac{k'_i}{k''_0} = \frac{i_s}{i!(nv_t)^i} \quad (2.17)$$

Therefore, maximizing i_{out} is equivalent to maximizing the target function

$$z_{\text{DC}} = \sum_{i \text{ even}, i \geq 2}^{n_o} k_i R_{\text{ant}}^{i/2} \mathbb{E}[y(t)^i] \quad (2.18)$$

2.3 Receiver Architectures

We investigated two practical architectures for the co-located integrated information and energy receiver. Both designs are equipped with individual ID and EH receivers. The former is a conventional baseband demodulator while the latter can be implemented with the proposed rectifier structure in Section 2.2.

2.3.1 Time Switching

A *Time Switching* (TS) receiver (Fig. 2.4) operates as either an information decoder or an energy harvester at a fixed time. In the design, the transmitter divides the transmission block into orthogonal power and data slots with length ratios α and $1 - \alpha$ respectively. It then optimizes the waveform for WPT or WIT individually. On the other hand, the receiver periodically switches between ID and EH receivers in the corresponding slots. Perfect synchronization between transmitter and receiver is required for precise mode control. It can achieve different rate-energy tradeoffs by adjusting the slot length ratio α jointly with the transmit signals. Since the information decoder and energy harvester may work in different power ranges, TS can be combined with a "near-far" scheduling [8] to benefit the system efficiency.

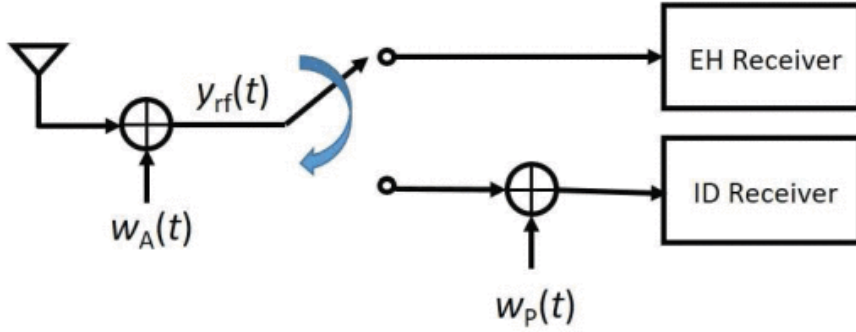


Figure 2.4: Structure of TS receiver [4]

2.3.2 Power Splitting

In *Power Splitting* (PS) receiver (Fig. 2.5), we introduce a PS ratio ρ to split the received signal into individual power stream (with proportion ρ) and information stream (with proportion $1 - \rho$). At the transmitter, the signal is jointly optimized for information and power transmission according to CSIT. When perfectly matched, the EH and ID receivers are with input voltage $\sqrt{\rho R_{ant}} y(t)$ and $\sqrt{(1 - \rho) R_{ant}} y(t)$ respectively. Different rate-energy pairs can be obtained by varying the PS ratio ρ . It is argued in [8] that PS is the best strategy for linear harvester model with negligible RF-to-baseband noise, but [3] demonstrated that the PS-only transmission is suboptimal when considering rectifier nonlinearity.

2.4 Signal and System Model

Consider a point-to-point MISO WIPT system in a multipath environment. The M -antenna transmitter delivers information and power simultaneously to the single-

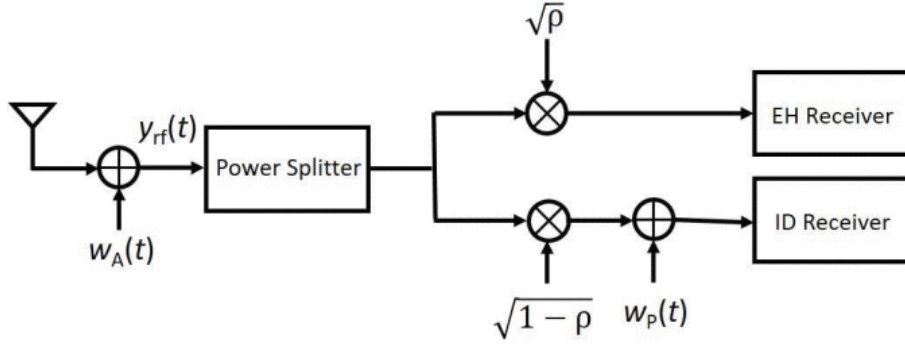


Figure 2.5: Structure of PS receiver [4]

antenna receiver through N orthogonal subbands. It is assumed the carrier frequencies are with even spacing Δf and equal bandwidth B_s . The n -th subband has carrier frequency $f_n = f_0 + n\Delta f$ for $n = 0, \dots, N-1$. To maximize the rate-energy trade-off, we employ a superposed signal consists of a multi-carrier deterministic multisine waveform and a multi-carrier modulated waveform for WIPT. Both components are transmitted on the same frequency bands.

2.4.1 Transmitted Information Waveform

Denoting the information symbol carried by the modulated waveform on subband n as \tilde{x}_n , we assume the input symbol is with the capacity-achieving i.i.d. Circular Symmetric Complex Gaussian (CSCG) distribution with zero mean and unit variance [35]:

$$\tilde{x}_n = |\tilde{x}_n| e^{j\phi_{\tilde{x}_n}} \sim \mathcal{CN}(0, 1) \quad (2.19)$$

Hence, the modulated waveform on antenna $m = 1, \dots, M$ subband $n = 1, \dots, N$ writes as

$$x_{n,m} = w_{I,n,m} \tilde{x}_n \quad (2.20)$$

where $w_{I,n,m}$ is the corresponding information weight and is a constant for a certain channel realization:

$$w_{I,n,m} = |w_{I,n,m}| e^{j\phi_{I,n,m}} = s_{I,n,m} e^{j\phi_{I,n,m}} \quad (2.21)$$

Note the amplitude and phase are separated in the optimization. Define matrices \mathbf{S}_I and $\mathbf{\Phi}_I$ of size $N \times M$ such that the (n, m) entries hold $s_{I,n,m}$ and $\phi_{I,n,m}$ respectively. In this way, the design of information waveform is converted into an optimization problem on both matrices, with the average WIT transmit power $P_I = \frac{1}{2} \|\mathbf{S}_I\|_F^2$. The modulated symbol (2.20) can be further expressed as

$$x_{n,m} = s_{I,n,m} e^{j\phi_{I,n,m}} \cdot |\tilde{x}_n| e^{j\phi_{\tilde{x}_n}} = \tilde{s}_{I,n,m} e^{j\tilde{\phi}_{I,n,m}} \quad (2.22)$$

with $\tilde{s}_{I,n,m} = s_{I,n,m} |\tilde{x}_n|$ and $\tilde{\phi}_{I,n,m} = \phi_{I,n,m} + \phi_{\tilde{x}_n}$. In this way, the impact of symbol distribution and waveform design are combined. The modulated waveform also follows an i.i.d. CSCG distribution with variance equal to the subband power $x_{n,m} \sim \mathcal{CN}(0, s_{I,n,m}^2)$.

Therefore, the information waveform $x_{I,m}(t)$ on antenna m at time t writes as

$$x_{I,m}(t) = \sum_{n=0}^{N-1} \tilde{s}_{I,n,m}(t) \cos(2\pi f_n t + \tilde{\phi}_{I,n,m}(t)) \quad (2.23)$$

$$= \Re \left\{ \sum_{n=0}^{N-1} x_{n,m}(t) e^{j2\pi f_n t} \right\} \quad (2.24)$$

$$= \Re \left\{ \sum_{n=0}^{N-1} w_{I,n,m} \tilde{x}_n(t) e^{j2\pi f_n t} \right\} \quad (2.25)$$

On top of this, the WIT signal vector is spread over M antennas

$$\mathbf{x}_I(t) = \Re \left\{ \sum_{n=0}^{N-1} \mathbf{w}_{I,n} \tilde{x}_n(t) e^{j2\pi f_n t} \right\} \quad (2.26)$$

where $\mathbf{w}_{I,n} = [w_{I,n,1} \cdots w_{I,n,M}]^T$.

2.4.2 Transmitted Power Waveform

Comparing with the information component, the multisine power component is unmodulated and deterministic, so there is no dependency on the distribution of input symbol $\tilde{x}_n(t)$. The power waveform on antenna m , subband n is given by

$$w_{P,n,m} = s_{P,n,m} e^{j\phi_{P,n,m}} \quad (2.27)$$

where $s_{P,n,m}$ and $\phi_{P,n,m}$ are the amplitude and phase of the multisine signal. Collecting them into the (n, m) entries of matrices \mathbf{S}_P and $\mathbf{\Phi}_P$, the average power of the WPT waveform equals $\frac{1}{2} \|\mathbf{S}_P\|_F^2$. Similarly, the power waveform $x_{P,m}(t)$ on antenna m at time t is

$$x_{P,m}(t) = \sum_{n=0}^{N-1} s_{P,n,m} \cos(2\pi f_n t + \phi_{P,n,m}) \quad (2.28)$$

$$= \Re \left\{ \sum_{n=0}^{N-1} w_{P,n,m} e^{j2\pi f_n t} \right\} \quad (2.29)$$

Combining the power signals on all M antennas, the WPT signal vector writes as

$$\mathbf{x}_P(t) = \Re \left\{ \sum_{n=0}^{N-1} \mathbf{w}_{P,n} e^{j2\pi f_n t} \right\} \quad (2.30)$$

with $\mathbf{w}_{P,n} = [w_{P,n,1} \cdots w_{P,n,M}]^T$.

2.4.3 Channel and Received Waveform

Consider a multipath channel with L paths. For the l -th path ($l = 1, \dots, L$), denote the phase shift between the receive antenna and transmit antenna m of subband n as $\zeta_{n,m,l}$. Let τ_l and α_l be the delay and magnitude gain, and indicate the transmit signal on subband n of antenna m as

$$v_{n,m}(t) = w_{P,n,m} + w_{I,n,m}\tilde{x}_n(t) \quad (2.31)$$

The superposed signal containing modulated information waveform and multi-sine power waveform is demonstrated to bring a two-fold benefit on rate and energy [4]. Also, the channel frequency response is expressed as

$$h_{n,m} = \sum_{l=0}^{L-1} \alpha_l e^{j(-2\pi f_n \tau_l + \zeta_{n,m,l})} = A_{n,m} e^{j\bar{\psi}_{n,m}} \quad (2.32)$$

We assume $\max_{l \neq l'} |\tau_l - \tau_{l'}| < 1/B_s$ to ensure $v_{n,m}(t)$ and $\tilde{x}_n(t)$ being narrow-band signals. It is also supposed that $v_{n,m}(t - \tau_l) = v_{n,m}(t)$ and $\tilde{x}_n(t - \tau_l) = \tilde{x}_n(t)$. The received signal corresponding to transmit antenna m contains the power component $y_{P,m}(t)$ and the information component $y_{I,m}(t)$

$$y_m(t) = y_{P,m}(t) + y_{I,m}(t) \quad (2.33)$$

$$= \Re \left\{ \sum_{l=0}^{L-1} \sum_{n=0}^{N-1} \alpha_l v_{n,m}(t - \tau_l) e^{j2\pi f_n(t - \tau_l) + \zeta_{n,m,l}} \right\} \quad (2.34)$$

$$\approx \Re \left\{ \sum_{n=0}^{N-1} h_{n,m} v_{n,m}(t) e^{j2\pi f_n t} \right\} \quad (2.35)$$

Hence, the total received signal can be obtained by stacking up (2.33) over all transmit signals

$$y(t) = y_P(t) + y_I(t) \quad (2.36)$$

$$= \Re \left\{ \sum_{n=0}^{N-1} \mathbf{h}_n (\mathbf{w}_{P,n} + \mathbf{w}_{I,n} \tilde{x}_n) e^{j2\pi f_n t} \right\} \quad (2.37)$$

where the channel vector is defined as $\mathbf{h}_n = [h_{n,1} \dots h_{n,M}]$.

2.4.4 Information Decoder

In the superposed transmit signal $x_m(t)$, the modulated component $x_{I,m}(t)$ carries all the information while the multisine component $x_{P,m}(t)$ completely serves the power. Since the latter is deterministic, it creates no interference and has zero contribution to the different entropy of $x_m(t)$ in terms of translation. Therefore, the achievable rate is equal to

$$I(\mathbf{S}_I, \Phi_I, \rho) = \sum_{n=0}^{N-1} \log_2 \left(1 + \frac{(1 - \rho) |\mathbf{h}_n \mathbf{w}_{I,n}|^2}{\sigma_n^2} \right) \quad (2.38)$$

where σ_n^2 is the total variance of the Gaussian noise at the RF-band and the noise introduced during the RF-to-baseband conversion (assumed Gaussian) on tone n . It reaches the maximum rate $I(\mathbf{S}_I^*, \mathbf{\Phi}_I^*, 0)$ and boils down to WIT by setting $\rho = 0$ then performing Maximum Ratio Transmission (MRT) and Water-Filling (WF) power allocation on subbands.

A significant conclusion in [11] is that the rate (2.38) is achievable with and without waveform cancellation. Since the multisine is deterministic, it can either be subtracted from the baseband signal or be used to construct the translated codebook. Conventional demodulation can be performed then.

2.4.5 Energy Harvester

To investigate the impact of the proposed waveform on the harvested power, we apply the received signal expression (2.33) to the diode current equation (2.14).

First, we consider the multi-carrier multisine waveform $y_P(t)$. The approximated harvester DC current with multisine excitation writes as

$$i_{\text{out}} \approx k'_0 + \sum_{\substack{i \text{ even}, i \geq 2}}^{n_o} k'_i \rho^{i/2} R_{\text{ant}}^{i/2} \mathbb{E} [y_P(t)^i] \quad (2.39)$$

The expectations of the received power waveform to the second and fourth orders were derived in [3] as

$$\mathbb{E} [y_P(t)^2] = \frac{1}{2} \sum_{n=0}^{N-1} |\mathbf{h}_n \mathbf{w}_{P,n}|^2 \quad (2.40)$$

$$= \frac{1}{2} \sum_{n=0}^{N-1} \sum_{m_0, m_1} s_{P,n,m_0} s_{P,n,m_1} A_{n,m_0} A_{n,m_1} \cos(\psi_{P,n,m_0} - \psi_{P,n,m_1}) \quad (2.41)$$

$$\mathbb{E} [y_P(t)^4] = \frac{3}{8} \Re \left\{ \sum_{\substack{n_0, n_1, n_2, n_3 \\ n_0 + n_1 = n_2 + n_3}} \mathbf{h}_{n_0} \mathbf{w}_{P,n_0} \mathbf{h}_{n_1} \mathbf{w}_{P,n_1} (\mathbf{h}_{n_2} \mathbf{w}_{P,n_2})^* (\mathbf{h}_{n_3} \mathbf{w}_{P,n_3})^* \right\} \quad (2.42)$$

$$= \frac{3}{8} \sum_{\substack{n_0, n_1, n_2, n_3 \\ n_0 + n_1 = n_2 + n_3}} \sum_{m_0, m_1, m_2, m_3} \left[\prod_{j=0}^3 s_{P,n_j, m_j} A_{n_j, m_j} \right] \cos(\psi_{P,n_0, m_0} + \psi_{P,n_1, m_1} - \psi_{P,n_2, m_2} - \psi_{P,n_3, m_3}) \quad (2.43)$$

We then turn to the multi-carrier modulated waveform $y_I(t)$. It can be treated as a multisine waveform for the input symbols $\{\tilde{x}_n\}$ that vary randomly with symbol rate $1/B_s$. Similarly, the approximated DC current provided by the rectifier is given by

$$i_{\text{out}} \approx k'_0 + \sum_{\substack{i \text{ even}, i \geq 2}}^{n_o} k'_i \rho^{i/2} R_{\text{ant}}^{i/2} \mathbb{E}_{\{\tilde{x}_n\}} [y_I(t)^i] \quad (2.44)$$

To obtain the expectation, we first extract the DC currents corresponding to a given set of amplitudes $\{\tilde{s}_{I,n,m}\}$ and phases $\{\tilde{\phi}_{I,n,m}\}$, then take the expectation

over the distribution of the input symbol \tilde{x}_n . As an i.i.d. CSCG distribution $\tilde{x}_n \sim \mathcal{CN}(0, 1)$ is assumed, the amplitude square $|\tilde{x}_n|^2$ is exponentially distributed with $\mathbb{E}[|\tilde{x}_n|^2] = 1$. Using the moment generating function, we also have

$$\mathbb{E}[|\tilde{x}_n|^4] = \mathbb{E}\left[\left(|\tilde{x}_n|^2\right)^2\right] = 2 \quad (2.45)$$

Note this modulation gain applies to the output current, which measures the contribution of modulation and does not exist for multisine waveform. Following [11], we can obtain the expectation of the received information waveform to the second and fourth orders

$$\mathbb{E}[y_I(t)^2] = \frac{1}{2} \sum_{n=0}^{N-1} \sum_{m_0, m_1} s_{I,n,m_0} s_{I,n,m_1} A_{n,m_0} A_{n,m_1} \cos(\psi_{I,n,m_0} - \psi_{I,n,m_1}) \quad (2.46)$$

$$= \frac{1}{2} \sum_{n=0}^{N-1} |\mathbf{h}_n \mathbf{w}_{I,n}|^2 \quad (2.47)$$

$$\mathbb{E}[y_I(t)^4] = \frac{6}{8} \sum_{n_0, n_1} \sum_{m_0, m_1, m_2, m_3} \left[\prod_{j=0,2} s_{I,n_0,m_j} A_{n_0,m_j} \right] \left[\prod_{j=1,3} s_{I,n_1,m_j} A_{n_1,m_j} \right] \cos(\psi_{I,n_0,m_0} + \psi_{I,n_1,m_1} - \psi_{I,n_0,m_2} - \psi_{I,n_1,m_3}) \quad (2.48)$$

$$= \frac{6}{8} \left[\sum_{n=0}^{N-1} |\mathbf{h}_n \mathbf{w}_{I,n}|^2 \right]^2 \quad (2.49)$$

It is worth noting that the truncation order n_o in (2.44) determines the relationship between the received signal and the harvested power. On top of it, [3] proposed two diode models:

- *diode linear model* ($n_o = 2$) is the conventional perspective that assumes the total output power is the sum of the subband power. It omits the rectifier nonlinearity and is typically suitable for very low input power (below -30 dBm).
- *diode nonlinear model* ($n_o > 2$) considers the contributions of higher-order terms to the harvested power. It captures the nonlinear behavior of the diode with the product terms modeling the cross contribution of different frequencies (as indicated by n_0, n_1 in (2.48) and (2.42)). The model is complicated but accurate, which especially fits the low power regime between -30 dBm and 0 dBm.

In the diode linear model corresponding to (2.40) and (2.46), the output current is only a function of $\sum_{n=0}^{N-1} |\mathbf{h}_n \mathbf{w}_{P/I,n}|^2$. Hence, it appears that multi-carrier multisine and modulated waveforms are equally suitable for WPT. On the other hand, the diode nonlinear model highlights a clear difference between the power delivered by both waveforms. For the modulated component, the second and fourth order terms in (2.46) and (2.48) share same dependencies on $\sum_{n=0}^{N-1} |\mathbf{h}_n \mathbf{w}_{I,n}|^2$. It implies that for a

modulated waveform with CSCG inputs, the higher order terms behave similarly to the second order term, and there is no essential difference between both models. In comparison, for the multisine waveform, the parts (2.40) and (2.42) are decomposed as the product of contributions from different subbands. Also, the second order term is linear as a sum over each frequency while the nonlinear fourth order term shows some cross correlation between different subbands.

In this paper, we set $n_o = 4$ to explore the fundamental nonlinear behaviour of the diode and its impact on the harvested current. Therefore, the approximated output DC current (2.14) reduces to

$$\begin{aligned} i_{\text{out}} \approx & k'_0 + k'_2 \rho R_{\text{ant}} \mathbb{E} [y_P(t)^2] + k'_4 \rho^2 R_{\text{ant}}^2 \mathbb{E} [y_P(t)^4] \\ & + k'_2 \rho R_{\text{ant}} \mathbb{E} [y_I(t)^2] + k'_4 \rho^2 R_{\text{ant}}^2 \mathbb{E} [y_I(t)^4] \\ & + 6k'_4 \rho^2 R_{\text{ant}}^2 \mathbb{E} [y_P(t)^2] \mathbb{E} [y_I(t)^2] \end{aligned} \quad (2.50)$$

whose corresponding target function is

$$\begin{aligned} z_{\text{DC}} \approx & k_0 + k_2 \rho R_{\text{ant}} \mathbb{E} [y_P(t)^2] + k_4 \rho^2 R_{\text{ant}}^2 \mathbb{E} [y_P(t)^4] \\ & + k_2 \rho R_{\text{ant}} \mathbb{E} [y_I(t)^2] + k_4 \rho^2 R_{\text{ant}}^2 \mathbb{E} [y_I(t)^4] \\ & + 6k_4 \rho^2 R_{\text{ant}}^2 \mathbb{E} [y_P(t)^2] \mathbb{E} [y_I(t)^2] \end{aligned} \quad (2.51)$$

Chapter 3

Rate-Energy Tradeoff

In this section, we first define the rate-energy (R-E) region for the proposed system, then formulate the characterization into a general optimization problem. On top of it, we decouple the spatial and frequency design, investigate the lower bound of the superposed waveform, consider the PAPR constraint, and extend the approach to MIMO cases.

3.1 Rate-Energy Region

The achievable R-E region is defined as

$$C_{R-I_{DC}}(P) \triangleq \left\{ (R, I_{DC}) : R \leq I, I_{DC} \leq i_{\text{out}}, \frac{1}{2} [\|\mathbf{S}_P\|_F^2 + \|\mathbf{S}_I\|_F^2] \leq P \right\} \quad (3.1)$$

where (R, I_{DC}) is the rate-energy pair, P is the average transmit power budget, I is the mutual information, I_{DC} is the harvested DC current, i_{out} is the rectifier output current, and $\mathbf{S}_P, \mathbf{S}_I$ hold the amplitudes of power and information signals respectively. Using the target function z_{DC} in (2.51), we redefine the R-E region as

$$C_{R-I_{DC}}(P) \triangleq \left\{ (R, I_{DC}) : R \leq I, I_{DC} \leq z_{DC}, \frac{1}{2} [\|\mathbf{S}_P\|_F^2 + \|\mathbf{S}_I\|_F^2] \leq P \right\} \quad (3.2)$$

The best R-E tradeoff can be achieved with the optimal amplitudes $\mathbf{S}_P^*, \mathbf{S}_I^*$ and phases Φ_P^*, Φ_I^* at the transmitter, together with the optimal power splitting ratio ρ^* at the receiver. It is assumed in the optimization that perfect CSI is available at the transmitter (in the form of channel frequency response $h_{n,m}$), and perfect synchronization is established between the transmitter and the receiver.

3.2 Problem Formulation

For the MISO case, the optimal phases to maximize the target function (2.51) and the mutual information (2.38) correspond to the phases of the matched filters

$$\phi_{P,n,m}^* = \phi_{I,n,m}^* = -\bar{\psi}_{n,m} \quad (3.3)$$

Such a decision can maximize all cosine terms in (2.40) – (2.49) by setting the arguments to 0. Φ_P^* and Φ_I^* can be constructed by collecting $\phi_{P,n,m}^*$ and $\phi_{I,n,m}^*$ to the (n, m) entries respectively. On top of it, the target function $z_{DC}(\mathbf{S}_P, \mathbf{S}_I, \Phi_P^*, \Phi_I^*, \rho)$ can be further written as

$$\begin{aligned}
z_{DC} = & \frac{k_2\rho}{2} R_{\text{ant}} \sum_{n=0}^{N-1} \sum_{m_0, m_1} \left[\prod_{j=0}^1 s_{P,n,m_j} A_{n,m_j} \right] \\
& + \frac{3k_4\rho^2}{8} R_{\text{ant}}^2 \sum_{\substack{n_0, n_1, n_2, n_3 \\ n_0+n_1=n_2+n_3}} \sum_{m_0, m_1, m_2, m_3} \left[\prod_{j=0}^3 s_{P,n_j,m_j} A_{n_j,m_j} \right] \\
& + \frac{k_2\rho}{2} R_{\text{ant}} \sum_{n=0}^{N-1} \sum_{m_0, m_1} \left[\prod_{j=0}^1 s_{I,n,m_j} A_{n,m_j} \right] \\
& + \frac{3k_4\rho^2}{4} R_{\text{ant}}^2 \sum_{n_0, n_1} \sum_{m_0, m_1, m_2, m_3} \left[\prod_{j=0,2} s_{I,n_0,m_j} A_{n_0,m_j} \right] \left[\prod_{j=1,3} s_{I,n_1,m_j} A_{n_1,m_j} \right] \\
& + \frac{3k_4\rho^2}{2} R_{\text{ant}}^2 \left[\sum_{n=0}^{N-1} \sum_{m_0, m_1} \left[\prod_{j=0}^1 s_{P,n,m_j} A_{n,m_j} \right] \right] \left[\sum_{n=0}^{N-1} \sum_{m_0, m_1} \left[\prod_{j=0}^1 s_{I,n,m_j} A_{n,m_j} \right] \right]
\end{aligned} \tag{3.4}$$

Also, with the optimum phases Φ_I^* , the mutual information I can be rewritten as

$$I(\mathbf{S}_I, \Phi_I^*, \rho) = \log_2 \left(\prod_{n=0}^{N-1} \left(1 + \frac{(1-\rho)}{\sigma_n^2} C_n \right) \right) \tag{3.5}$$

with $C_n = \sum_{m_0, m_1} \prod_{j=0}^1 s_{I,n,m_j} A_{n,m_j}$.

It is also demonstrated in [33] that using a matched filter for power allocation can lead to a suboptimal performance with much lower complexity. Therefore, it is employed to initialize the iterative algorithms for fast convergence. On antenna m and subband n , the amplitudes of power and information waveform are initialized to

$$s_{P,n,m} = s_{I,n,m} = cA_{n,m} \tag{3.6}$$

where c is the coefficient to guarantee the transmit power constraint.

With the optimum phases Φ_P^* and Φ_I^* , both the target function (3.4) and mutual information (3.5) are posynomials [36]. Therefore, we can convert the characterization of R-E region into an energy maximization problem with average transmit power budget P and rate constraint \bar{R}

$$\max_{\mathbf{S}_P, \mathbf{S}_I, \rho} z_{DC}(\mathbf{S}_P, \mathbf{S}_I, \Phi_P^*, \Phi_I^*, \rho) \tag{3.7}$$

$$\text{subject to} \quad \frac{1}{2} [\|\mathbf{S}_I\|_F^2 + \|\mathbf{S}_P\|_F^2] \leq P, \tag{3.8}$$

$$I(\mathbf{S}_I, \Phi_I^*, \rho) \geq \bar{R} \tag{3.9}$$

In the following section, we transform the optimization into standard Geometric Programming (GP) problems and consider different settings and constraints.

3.3 Iterative Algorithms

3.3.1 General Approach

Although the problem (3.7) – (3.9) is not a standard GP, we can transform it to a Reversed GP by introducing an auxiliary variable t_0 [37]

$$\min_{\mathbf{S}_P, \mathbf{S}_I, \rho, t_0} \quad 1/t_0 \quad (3.10)$$

$$\text{subject to} \quad \frac{1}{2} [\|\mathbf{S}_I\|_F^2 + \|\mathbf{S}_P\|_F^2] \leq P \quad (3.11)$$

$$t_0/z_{DC}(\mathbf{S}_P, \mathbf{S}_I, \Phi_P^*, \Phi_I^*, \rho) \leq 1 \quad (3.12)$$

$$2^{\bar{R}} / \left[\prod_{n=0}^{N-1} \left(1 + \frac{(1-\rho)}{\sigma_n^2} C_n \right) \right] \leq 1 \quad (3.13)$$

We cannot apply GP tools to the new problem yet, as $1/z_{DC}(\mathbf{S}_P, \mathbf{S}_I, \Phi_P^*, \Phi_I^*, \rho)$ and $1/\left[\prod_{n=0}^{N-1} \left(1 + \frac{(1-\rho)}{\sigma_n^2} C_n \right)\right]$ are not posynomials. To solve this, [11] suggested a conservative approach to approximate the terms with posynomials in the denominator by new posynomials, based on the Arithmetic Mean-Geometric Mean (AM-GM) inequality.

Consider constraint (3.12) first. The posynomial at the denominator can be decomposed as the sum of monomials

$$z_{DC}(\mathbf{S}_P, \mathbf{S}_I, \Phi_P^*, \Phi_I^*, \rho) = \sum_{k=1}^K g_k(\mathbf{S}_P, \mathbf{S}_I, \Phi_P^*, \Phi_I^*, \rho) \quad (3.14)$$

Since monomial $\{g_k\}$ is nonnegative for all k , the AM-GM inequality suggests a posynomial upper bound for the previous non-posynomial term

$$\frac{1}{\sum_{k=1}^K g_k(\mathbf{S}_P, \mathbf{S}_I, \Phi_P^*, \Phi_I^*, \rho)} \leq \prod_{k=1}^K \left(\frac{g_k(\mathbf{S}_P, \mathbf{S}_I, \Phi_P^*, \Phi_I^*, \rho)}{\gamma_k} \right)^{-\gamma_k} \quad (3.15)$$

The nonnegative coefficients $\{\gamma_k\}$ are chosen to satisfy $\sum_{k=1}^K \gamma_k = 1$. Similarly, define $\bar{\rho} = 1 - \rho$ and let $\{g_{nk}(\mathbf{S}_I, \bar{\rho})\}$ be the monomials of the posynomial $1 + \frac{\bar{\rho}}{\sigma_n^2} C_n$, we have

$$1 + \frac{\bar{\rho}}{\sigma_n^2} C_n = \sum_{k=1}^{K_n} g_{nk}(\mathbf{S}_I, \bar{\rho}) \quad (3.16)$$

Apply the AM-GM inequality to (3.16), we have

$$\frac{1}{1 + \frac{\bar{\rho}}{\sigma_n^2} C_n} \leq \prod_{k=1}^{K_n} \left(\frac{g_{nk}(\mathbf{S}_I, \bar{\rho})}{\gamma_{nk}} \right)^{-\gamma_{nk}} \quad (3.17)$$

with $\gamma_{nk} \geq 0$ and $\sum_{k=1}^{K_n} \gamma_{nk} = 1$. In this way, we transformed the problem into a standard GP

$$\min_{\mathbf{S}_P, \mathbf{S}_I, \rho, \bar{\rho}, t_0} 1/t_0 \quad (3.18)$$

$$\text{subject to} \quad \frac{1}{2} [\|\mathbf{S}_I\|_F^2 + \|\mathbf{S}_P\|_F^2] \leq P \quad (3.19)$$

$$t_0 \prod_{k=1}^K \left(\frac{g_k(\mathbf{S}_P, \mathbf{S}_I, \Phi_P^*, \Phi_I^*, \rho)}{\gamma_k} \right)^{-\gamma_k} \leq 1 \quad (3.20)$$

$$2^{\bar{R}} \prod_{n=0}^{N-1} \prod_{k=1}^{K_n} \left(\frac{g_{nk}(\mathbf{S}_I, \bar{\rho})}{\gamma_{nk}} \right)^{-\gamma_{nk}} \leq 1 \quad (3.21)$$

$$\rho + \bar{\rho} \leq 1 \quad (3.22)$$

It is worth noting that the tightness of the AM-GM inequality depends on the choice of $\{\gamma_k, \gamma_{nk}\}$. In this paper, we employ the iterative method proposed in [11] that updates the coefficient sets at iteration i with the previous solution $\mathbf{S}_P^{(i-1)}, \mathbf{S}_I^{(i-1)}, \rho^{(i-1)}$ by

$$\gamma_k = \frac{g_k(\mathbf{S}_P^{(i-1)}, \mathbf{S}_I^{(i-1)}, \rho^{(i-1)})}{z_{DC}(\mathbf{S}_P^{(i-1)}, \mathbf{S}_I^{(i-1)}, \rho^{(i-1)})}, \quad k = 1, \dots, K \quad (3.23)$$

$$\gamma_{nk} = \frac{g_{nk}(\mathbf{S}_I^{(i-1)}, \bar{\rho}^{(i-1)})}{1 + \frac{\bar{\rho}^{(i-1)}}{\sigma_n^2} C_n(\mathbf{S}_I^{(i-1)})}, \quad n = 0, \dots, N-1, k = 1, \dots, K_n \quad (3.24)$$

Once $\{\gamma_k, \gamma_{nk}\}$ are obtained, we solve (3.18) – (3.22) to obtain $\mathbf{S}_P^{(i)}, \mathbf{S}_I^{(i)}, \rho^{(i)}$. The iteration is repeated until it converges. Algorithm 1 summarizes the procedures involved in the optimization. The successive approximation approach is also known as inner approximation method [38], which cannot guarantee a global optimal solution but the result point satisfies the Karush–Kuhn–Tucker (KKT) conditions.

Algorithm 1 General Waveform Design

- 1: **Initialize:** $i \leftarrow 0$, Φ_P^*, Φ_I^* in (3.3), $\mathbf{S}_P, \mathbf{S}_I$ in (3.6), $\rho, \bar{\rho} = 1 - \rho$, $\bar{R}, z_{DC}^{(0)} = 0$
 - 2: **repeat**
 - 3: $i \leftarrow i + 1, \ddot{\mathbf{S}}_P \leftarrow \mathbf{S}_P, \ddot{\mathbf{S}}_I \leftarrow \mathbf{S}_I, \ddot{\rho} \leftarrow \rho, \ddot{\bar{\rho}} \leftarrow \bar{\rho}$
 - 4: $\gamma_k \leftarrow g_k(\ddot{\mathbf{S}}_P, \ddot{\mathbf{S}}_I, \Phi_P^*, \Phi_I^*, \ddot{\rho}) / z_{DC}(\ddot{\mathbf{S}}_P, \ddot{\mathbf{S}}_I, \Phi_P^*, \Phi_I^*, \ddot{\rho}), k = 1, \dots, K$
 - 5: $\gamma_{nk} \leftarrow g_{nk}(\ddot{\mathbf{S}}_I, \ddot{\bar{\rho}}) / \left(1 + \frac{\ddot{\bar{\rho}}}{\sigma_n^2} C_n(\ddot{\mathbf{S}}_I)\right), n = 0, \dots, N-1, k = 1, \dots, K_n$
 - 6: $\mathbf{S}_P, \mathbf{S}_I, \rho, \bar{\rho} \leftarrow \arg \min (3.18) - (3.22)$
 - 7: $z_{DC}^{(i)} \leftarrow z_{DC}(\mathbf{S}_P, \mathbf{S}_I, \Phi_P^*, \Phi_I^*, \rho)$
 - 8: **until** $|z_{DC}^{(i)} - z_{DC}^{(i-1)}| < \epsilon$ or $i = i_{\max}$
-

3.3.2 Decoupled Design

For the transmitter with multiple antennas ($M > 1$), the previous method is involved with weight design across space and frequency. In this part, we will investigate an approach proposed in [11] that decouples the optimization in spatial

and frequency domains without impacting performance. As suggested by (2.38) and (2.40) – (2.49), the optimum weight vectors $\mathbf{w}_{P,n}$ and $\mathbf{w}_{I,n}$ that maximize the rate and energy correspond to the MRT beamformers, which are given by

$$\mathbf{w}_{P,n} = s_{P,n} \mathbf{h}_n^H / \|\mathbf{h}_n\| \quad (3.25)$$

$$\mathbf{w}_{I,n} = s_{I,n} \mathbf{h}_n^H / \|\mathbf{h}_n\| \quad (3.26)$$

Therefore, the received power and information signals (2.36) rewrites as

$$y_P(t) = \sum_{n=0}^{N-1} \|\mathbf{h}_n\| s_{P,n} \cos(w_n t) = \Re \left\{ \sum_{n=0}^{N-1} \|\mathbf{h}_n\| s_{P,n} e^{jw_n t} \right\} \quad (3.27)$$

$$y_I(t) = \sum_{n=0}^{N-1} \|\mathbf{h}_n\| s_{I,n} \tilde{x}_n \cos(w_n t) = \Re \left\{ \sum_{n=0}^{N-1} \|\mathbf{h}_n\| s_{I,n} \tilde{x}_n e^{jw_n t} \right\} \quad (3.28)$$

In this way, the weight optimization on multiple transmit antennas is converted into an equivalent problem on a single antenna. For the n -th subband, the equivalent channel gain is $\|\mathbf{h}_n\|$ with the power allocated to multisine and modulated waveform denoted by $s_{P,n}^2$ and $s_{I,n}^2$ ($\frac{1}{2} \sum_{n=0}^{N-1} (s_{P,n}^2 + s_{I,n}^2) \leq P$). The problem can be solved using Algorithm 1, with the second and fourth order terms reduced to

$$\mathbb{E} [y_P(t)^2] = \frac{1}{2} \sum_{n=0}^{N-1} \|\mathbf{h}_n\|^2 s_{P,n}^2 \quad (3.29)$$

$$\mathbb{E} [y_P(t)^4] = \frac{3}{8} \sum_{\substack{n_0, n_1, n_2, n_3 \\ n_0 + n_1 = n_2 + n_3}} \left[\prod_{j=0}^3 s_{P, n_j} \|\mathbf{h}_{n_j}\| \right] \quad (3.30)$$

$$\mathbb{E} [y_I(t)^2] = \frac{1}{2} \sum_{n=0}^{N-1} \|\mathbf{h}_n\|^2 s_{I,n}^2 \quad (3.31)$$

$$\mathbb{E} [y_I(t)^4] = \frac{6}{8} \left[\sum_{n=0}^{N-1} \|\mathbf{h}_n\|^2 s_{I,n}^2 \right]^2 \quad (3.32)$$

Hence, the target function z_{DC} is only a function of two N -dimensional vectors $\mathbf{s}_{P/I} = [s_{P/I,0}, \dots, s_{P/I,N-1}]$, and the mutual information I can be simplified as

$$I(\mathbf{s}_I, \rho) = \log_2 \left(\prod_{n=0}^{N-1} \left(1 + \frac{(1-\rho)}{\sigma_n^2} s_{I,n}^2 \|\mathbf{h}_n\|^2 \right) \right) \quad (3.33)$$

Similarly, we decompose the posynomials $z_{DC}(\mathbf{s}_P, \mathbf{s}_I, \rho) = \sum_{k=1}^K g_k(\mathbf{s}_P, \mathbf{s}_I, \rho)$ and $1 + \frac{\bar{\rho}}{\sigma_n^2} C_n = \sum_{k=1}^{K_n} g_{nk}(\mathbf{s}_I, \bar{\rho})$ with $C_n = s_{I,n}^2 \|\mathbf{h}_n\|^2$, then apply the AM-GM inequality to the constraints with posynomials in the denominator. The equivalent GP problem write as

$$\min_{\mathbf{s}_P, \mathbf{s}_I, \rho, \bar{\rho}, t_0} \quad 1/t_0 \quad (3.34)$$

$$\text{subject to} \quad \frac{1}{2} [\|\mathbf{s}_I\|^2 + \|\mathbf{s}_P\|^2] \leq P \quad (3.35)$$

$$t_0 \prod_{k=1}^K \left(\frac{g_k(\mathbf{s}_P, \mathbf{s}_I, \rho)}{\gamma_k} \right)^{-\gamma_k} \leq 1 \quad (3.36)$$

$$2^{\bar{R}} \prod_{n=0}^{N-1} \prod_{k=1}^{K_n} \left(\frac{g_{nk}(\mathbf{s}_I, \bar{\rho})}{\gamma_{nk}} \right)^{-\gamma_{nk}} \leq 1 \quad (3.37)$$

$$\rho + \bar{\rho} \leq 1 \quad (3.38)$$

Following (3.6), the amplitudes of power and information waveform can be initialized to

$$s_{P,n} = s_{I,n} = c \|\mathbf{h}_n\| \quad (3.39)$$

Compared with the general approach, the decoupled design guarantees the same performance by a joint space-frequency design with a lower computational complexity, which converts the original $N \times M$ matrices $\mathbf{S}_P, \mathbf{S}_I$ to N -dimensional vectors $\mathbf{s}_P, \mathbf{s}_I$ via MRT beamformers. Algorithm 2 summarizes the optimization process of the decoupling strategy.

Algorithm 2 Decoupled Waveform Design

- 1: **Initialize:** $i \leftarrow 0$, Φ_P^*, Φ_I^* in (3.3), $\mathbf{s}_P, \mathbf{s}_I$ in (3.39), $\rho, \bar{\rho} = 1 - \rho$, $\bar{R}, z_{DC}^{(0)} = 0$
 - 2: **repeat**
 - 3: $i \leftarrow i + 1$, $\ddot{\mathbf{s}}_P \leftarrow \mathbf{s}_P$, $\ddot{\mathbf{s}}_I \leftarrow \mathbf{s}_I$, $\ddot{\rho} \leftarrow \rho$, $\ddot{\bar{\rho}} \leftarrow \bar{\rho}$
 - 4: $\gamma_k \leftarrow g_k(\ddot{\mathbf{s}}_P, \ddot{\mathbf{s}}_I, \Phi_P^*, \Phi_I^*, \ddot{\rho}) / z_{DC}(\ddot{\mathbf{s}}_P, \ddot{\mathbf{s}}_I, \Phi_P^*, \Phi_I^*, \ddot{\rho})$, $k = 1, \dots, K$
 - 5: $\gamma_{nk} \leftarrow g_{nk}(\ddot{\mathbf{s}}_I, \ddot{\rho}) / \left(1 + \frac{\ddot{\rho}}{\sigma_n^2} C_n(\ddot{\mathbf{s}}_I)\right)$, $n = 0, \dots, N-1, k = 1, \dots, K_n$
 - 6: $\mathbf{s}_P, \mathbf{s}_I, \rho, \bar{\rho} \leftarrow \arg \min (3.34) - (3.38)$
 - 7: $z_{DC}^{(i)} \leftarrow z_{DC}(\mathbf{s}_P, \mathbf{s}_I, \Phi_P^*, \Phi_I^*, \rho)$
 - 8: **until** $|z_{DC}^{(i)} - z_{DC}^{(i-1)}| < \epsilon$ or $i = i_{\max}$
-

3.3.3 Lower Bound

The deterministic multisine waveform not only boosts the harvested energy but also avoids interference to the modulated waveform. To highlight its benefit on rate and energy, we compare the performance of superposed waveform to two baselines. In the first case, there is no multisine component. Only modulated waveform is used for WIPT (i.e. $\mathbf{S}_P = 0$, $\frac{1}{2} \|\mathbf{S}_I\|_F^2 = P$) and the twofold benefit disappears. In the second baseline, it is assumed that the power waveform behaves as a deterministic multisine from WPT perspective but as CSCG distributed from WIT perspective. Therefore, the energy benefit of the multisine is maintained but the rate benefit is lost. The power waveform creates an interference term $\sqrt{1 - \rho} \mathbf{h}_n \mathbf{w}_{P,n}$ to the information waveform, and the lower bound of the mutual information writes as

$$I_{LB}(\mathbf{S}_P, \mathbf{S}_I, \Phi_P, \Phi_I, \rho) = \sum_{n=0}^{N-1} \log_2 \left(1 + \frac{(1 - \rho) |\mathbf{h}_n \mathbf{w}_{I,n}|^2}{\sigma_n^2 + (1 - \rho) |\mathbf{h}_n \mathbf{w}_{P,n}|^2} \right) \quad (3.40)$$

It leads to a smaller rate-energy region than the ideal case. Also, the MRT beamformers $\mathbf{w}_{P,n}, \mathbf{w}_{I,n}$ in (3.25) are suboptimal due to the interference, and the corresponding phases Φ_P^*, Φ_I^* in (3.3) are not the best solution for $M > 1$. Minimum Mean Squared Error (MMSE) combiner can be further exploited for a better joint design over space and frequency domains.

Consider the suboptimal phases Φ_P^* and Φ_I^* in (3.3) for simplicity. In such cases, the target function is still as (2.51) while the lower bound of the achievable rate is now

$$I_{LB}(\mathbf{S}_I, \Phi_I^*, \rho) = \log_2 \left(\prod_{n=0}^{N-1} \left(1 + \frac{(1-\rho)C_n}{\sigma_n^2 + (1-\rho)D_n} \right) \right) \quad (3.41)$$

with $C_n = \sum_{m_0, m_1} \prod_{j=0}^1 s_{I,n,m_j} A_{n,m_j}$ and $D_n = \sum_{m_0, m_1} \prod_{j=0}^1 s_{P,n,m_j} A_{n,m_j}$. Thus, the previous rate constraint (3.13) is replaced by

$$2^{\bar{R}} \frac{\prod_{n=0}^{N-1} \left(1 + \frac{\bar{\rho}}{\sigma_n^2} D_n \right)}{\prod_{n=0}^{N-1} \left(1 + \frac{\bar{\rho}}{\sigma_n^2} (D_n + C_n) \right)} \leq 1 \quad (3.42)$$

Decompose the posynomials in the denominators as

$$1 + \frac{\bar{\rho}}{\sigma_n^2} (D_n + C_n) = \sum_{j=1}^{J_n} f_{nj}(\mathbf{S}_P, \mathbf{S}_I, \rho) \quad (3.43)$$

where $\{f_{nj}(\mathbf{S}_P, \mathbf{S}_I, \rho)\}$ is the monomial terms. With a proper choice of nonnegative $\{\gamma_{nj}\}$ satisfying $\sum_{j=1}^{J_n} \gamma_{nj} = 1$, the standard GP can be written as

$$\min_{\mathbf{S}_P, \mathbf{S}_I, \rho, \bar{\rho}, t_0} \quad 1/t_0 \quad (3.44)$$

$$\text{subject to} \quad \frac{1}{2} [\|\mathbf{S}_I\|_F^2 + \|\mathbf{S}_P\|_F^2] \leq P \quad (3.45)$$

$$t_0 \prod_{k=1}^K \left(\frac{g_k(\mathbf{S}_P, \mathbf{S}_I, \Phi_P^*, \Phi_I^*, \rho)}{\gamma_k} \right)^{-\gamma_k} \leq 1 \quad (3.46)$$

$$2^{\bar{R}} \prod_{n=0}^{N-1} \left(1 + \frac{\bar{\rho}}{\sigma_n^2} D_n(\mathbf{S}_P) \right) \prod_{j=1}^{J_n} \left(\frac{f_{nj}(\mathbf{S}_P, \mathbf{S}_I, \rho)}{\gamma_{nj}} \right)^{-\gamma_{nj}} \leq 1 \quad (3.47)$$

$$\rho + \bar{\rho} \leq 1 \quad (3.48)$$

Algorithm 3 shows the basic idea to obtain the lower-bound of R-E region. It boils down to Algorithm 1 when the interference posynomial $D_n = 0$ for all n .

3.3.4 PAPR Constraints

Another practical constraint at the transmitter is PAPR. We assume the modulated information waveform is with unit PAPR (by PSK or FSK) so that the limitation only influence the design of multisine power waveform. Following (2.28), the PAPR constraint on antenna m writes as

Algorithm 3 Lower-Bound of R-E Region

1: **Initialize:** $i \leftarrow 0$, $\mathbf{w}_{P,n}, \mathbf{w}_{I,n}$ in (3.25), $\mathbf{S}_P, \mathbf{S}_I$ in (3.6), $\rho, \bar{\rho} = 1 - \rho$, $\bar{R}, z_{DC}^{(0)} = 0$
 2: **repeat**
 3: $i \leftarrow i + 1, \ddot{\mathbf{S}}_P \leftarrow \mathbf{S}_P, \ddot{\mathbf{S}}_I \leftarrow \mathbf{S}_I, \ddot{\rho} \leftarrow \rho, \ddot{\bar{\rho}} \leftarrow \bar{\rho}$
 4: $\gamma_k \leftarrow g_k(\ddot{\mathbf{S}}_P, \ddot{\mathbf{S}}_I, \ddot{\rho}) / z_{DC}(\ddot{\mathbf{S}}_P, \ddot{\mathbf{S}}_I, \ddot{\rho}), k = 1, \dots, K$
 5: $\gamma_{nj} \leftarrow f_{nj}(\ddot{\mathbf{S}}_P, \ddot{\mathbf{S}}_I, \ddot{\rho}) / \left(1 + \frac{\ddot{\rho}}{\sigma_n^2} \left(D_n(\ddot{\mathbf{S}}_P) + C_n(\ddot{\mathbf{S}}_I)\right)\right)$
 6: $\mathbf{S}_P, \mathbf{S}_I, \rho, \bar{\rho} \leftarrow \arg \min (3.44) - (3.48)$
 7: $z_{DC}^{(i)} \leftarrow z_{DC}(\mathbf{S}_P, \mathbf{S}_I, \rho)$
 8: **until** $\left|z_{DC}^{(i)} - z_{DC}^{(i-1)}\right| < \text{or } i = i_{\max}$

$$\text{PAPR}_m = \frac{\max_t |x_{P,m}(t)|^2}{\mathbb{E}[|x_{P,m}(t)|^2]} = \frac{\max_t |x_{P,m}(t)|^2}{\frac{1}{2}\|\mathbf{s}_{P,m}\|^2} \leq \eta \quad (3.49)$$

We assume the optimum phases Φ_P^*, Φ_I^* in (3.3) are used in the optimization of $\mathbf{S}_I, \mathbf{S}_P$. To handle the PAPR constraint (3.49), we introduce an oversampling factor O_s to sample the power waveform at $t_q = qT/NO_s$ for $q = 0, \dots, NO_s - 1$ with $T = 1/\Delta f$. For a sufficiently large O_s , the PAPR constraint can be expressed as

$$|x_{P,m}(t_q)|^2 \leq \frac{1}{2}\eta\|\mathbf{s}_{P,m}\|^2 \quad (3.50)$$

where the l.h.s. obtained from equation (2.28) is

$$|x_{P,m}(t_q)|^2 = \sum_{n_0, n_1} s_{P,n_0,m} s_{P,n_1,m} \cos(w_{n_0} t_q + \phi_{P,n_0,m}^*) \cos(w_{n_1} t_q + \phi_{P,n_1,m}^*) \quad (3.51)$$

However, $|x_{P,m}(t_q)|^2$ is no longer a posynomial as some coefficients can be negative with time-varying arguments. It is named signomial [36] and can be decomposed either as the sum of monomials or as the difference of two posynomials

$$|x_{P,m}(t_q)|^2 = f_{mq}(\mathbf{S}_P, \Phi_P^*) = f_{mq1}(\mathbf{S}_P, \Phi_P^*) - f_{mq2}(\mathbf{S}_P, \Phi_P^*) \quad (3.52)$$

Therefore, the PAPR constraint rewrites as

$$\frac{f_{mq1}(\mathbf{S}_P, \Phi_P^*)}{\frac{1}{2}\eta\|\mathbf{s}_{P,m}\|^2 + f_{mq2}(\mathbf{S}_P, \Phi_P^*)} \leq 1 \quad (3.53)$$

Similarly, denote the posynomial at the denominator as

$$\frac{1}{2}\eta\|\mathbf{s}_{P,m}\|^2 + f_{mq2}(\mathbf{S}_P, \Phi_P^*) = \sum_{k=1}^{K_{mq2}} g_{mq2k}(\mathbf{S}_P, \Phi_P^*) \quad (3.54)$$

With a proper choice of nonnegative $\{\gamma_{mq2k}\}$ satisfying $\sum_{k=1}^{K_{mq2}} \gamma_{mq2k} = 1$, we apply AM-GM inequality to (3.53) and obtain the new constraint

$$f_{mq1}(\mathbf{S}_P, \Phi_P^*) \prod_{k=1}^{K_{mq2}} \left(\frac{g_{mq2k}(\mathbf{S}_P, \Phi_P^*)}{\gamma_{mq2k}} \right)^{-\gamma_{mq2k}} \leq 1 \quad (3.55)$$

In this way, the optimization problem (3.18) – (3.22) with an extra PAPR constraint (3.49) is replaced by a standard GP

$$\min_{\mathbf{S}_P, \mathbf{S}_I, \rho, \bar{\rho}, t_0} 1/t_0 \quad (3.56)$$

$$\text{subject to} \quad \frac{1}{2} [\|\mathbf{S}_I\|_F^2 + \|\mathbf{S}_P\|_F^2] \leq P \quad (3.57)$$

$$t_0 \prod_{k=1}^K \left(\frac{g_k(\mathbf{S}_P, \mathbf{S}_I, \Phi_P^*, \Phi_I^*, \rho)}{\gamma_k} \right)^{-\gamma_k} \leq 1 \quad (3.58)$$

$$2^{\bar{R}} \prod_{n=0}^{N-1} \prod_{k=1}^{K_n} \left(\frac{g_{nk}(\mathbf{S}_I, \bar{\rho})}{\gamma_{nk}} \right)^{-\gamma_{nk}} \leq 1 \quad (3.59)$$

$$f_{mq1}(\mathbf{S}_P, \Phi_P^*) \prod_{k=1}^{K_{mq2}} \left(\frac{g_{mq2k}(\mathbf{S}_P, \Phi_P^*)}{\gamma_{mq2k}} \right)^{-\gamma_{mq2k}} \leq 1 \quad (3.60)$$

$$\rho + \bar{\rho} \leq 1 \quad (3.61)$$

Algorithm 4 shows the gist of the optimization procedure. For the system with multiple transmit antenna and valid PAPR constraints, the decoupling strategy is suboptimal since the arguments of cosines are indeed frequency-dependent. Also, the multisine waveform is oversampled to satisfy the PAPR constraint, which further increases the overall computational complexity.

Algorithm 4 Waveform Design with PAPR Constraints

- 1: **Initialize:** $i \leftarrow 0$, Φ_P^*, Φ_I^* in (3.3), $\mathbf{S}_P, \mathbf{S}_I$ in (3.6), $\rho, \bar{\rho} = 1 - \rho$, $\bar{R}, z_{DC}^{(0)} = 0$
 - 2: **repeat**
 - 3: $i \leftarrow i + 1, \ddot{\mathbf{S}}_P \leftarrow \mathbf{S}_P, \ddot{\mathbf{S}}_I \leftarrow \mathbf{S}_I, \ddot{\rho} \leftarrow \rho, \ddot{\bar{\rho}} \leftarrow \bar{\rho}$
 - 4: $\gamma_k \leftarrow g_k(\ddot{\mathbf{S}}_P, \ddot{\mathbf{S}}_I, \Phi_P^*, \Phi_I^*, \ddot{\rho}) / z_{DC}(\ddot{\mathbf{S}}_P, \ddot{\mathbf{S}}_I, \Phi_P^*, \Phi_I^*, \ddot{\rho}), k = 1, \dots, K$
 - 5: $\gamma_{nk} \leftarrow g_{nk}(\ddot{\mathbf{S}}_I, \ddot{\rho}) / \left(1 + \frac{\ddot{\rho}}{\sigma_n^2} C_n(\ddot{\mathbf{S}}_I)\right), n = 0, \dots, N-1, k = 1, \dots, K_n$
 - 6: $\gamma_{mq2k} \leftarrow g_{mq2k}(\ddot{\mathbf{S}}_P, \Phi_P^*) / \left(\frac{1}{2}\eta \|\mathbf{s}_{P,m}\|^2 + f_{mq2}(\ddot{\mathbf{S}}_P, \Phi_P^*)\right),$
 $m = 1, \dots, M, q = 0, \dots, NO_s - 1, k = 1, \dots, K_{mq2}$
 - 7: $\mathbf{S}_P, \mathbf{S}_I, \rho, \bar{\rho} \leftarrow \arg \min (3.56) - (3.61)$
 - 8: $z_{DC}^{(i)} \leftarrow z_{DC}(\mathbf{S}_P, \mathbf{S}_I, \Phi_P^*, \Phi_I^*, \rho)$
 - 9: **until** $|z_{DC}^{(i)} - z_{DC}^{(i-1)}| < \epsilon$ or $i = i_{\max}$
-

3.3.5 Multiple Rectennas

The R-E region is expected to be enlarged by using multiple rectennas. In this part, we extend the general MISO strategy in [11] to U rectennas, which can either serve a single user in a point-to-point MIMO or spread across multiple users in an MU-MISO. Note that there exists a tradeoff between the energy harvested in different rectennas since they have different preference on the transmitted waveform. The fairness issue can be solved by introducing weight v_u for rectenna $u = 1, \dots, U$ and considering the weighted sum of DC components as a new target function

$$Z_{DC}(\mathbf{S}_P, \mathbf{S}_I, \Phi_P, \Phi_I, \rho) = \sum_{u=1}^U v_u z_{DC,u}(\mathbf{S}_P, \mathbf{S}_I, \Phi_P, \Phi_I, \rho) \quad (3.62)$$

With multiple rectennas, the frequency response is extended to

$$h_{n,m,u} = A_{n,m,u} e^{j\bar{\psi}_{n,m,u}} \quad (3.63)$$

Therefore, the phase of the received signal on rectenna u in subband n transmitted by antenna m equals

$$\psi_{n,m,u} = \phi_{n,m} + \bar{\psi}_{n,m,u} \quad (3.64)$$

where $\phi_{n,m}$ is the beamforming phase. In such cases, it is impossible to ensure $\psi_{n,m,u} = 0$ for all rectennas as there are three constraints n, m, u but only two variables n, m . With a specific phase design, the arguments of cosines in (2.40) – (2.49) are not guaranteed to be zero such that the target function Z_{DC} is indeed a signomial.

Denoting $\tilde{\mathbf{h}}_{n,u} = \sqrt{k_2 v_u} \mathbf{h}_{n,u}$, the channel matrix for subband n can be constructed as

$$\tilde{\mathbf{H}}_n = [\tilde{\mathbf{h}}_{n,1}^T \dots \tilde{\mathbf{h}}_{n,U}^T]^T \quad (3.65)$$

It is mentioned in [3] that a possible phase choice Φ'_P, Φ'_I is to set the (n, m) entries as

$$\phi'_{P,n,m} = \phi'_{I,n,m} = \angle v_{\max,n,m} \quad (3.66)$$

where $v_{\max,n,m}$ is the m -th term of the dominant right singular vector $\mathbf{v}_{\max,n}$ that can be obtained by singular value decomposition of $\tilde{\mathbf{H}}_n$. Also, the subband amplitudes can be initialized using the maximum eigenvalue λ_n

$$s_{P,n,m} = s_{I,n,m} = c\lambda_n \quad (3.67)$$

where c is the coefficient to guarantee the transmit power constraint. Note that the initialization is irrelevant to m .

To convert the problem into a standard GP, we introduce an auxiliary variable t_0 and rewrite the signomial as the difference of two posynomials

$$Z_{DC}(\mathbf{S}_P, \mathbf{S}_I, \Phi'_P, \Phi'_I, \rho) = f_1(\mathbf{S}_P, \mathbf{S}_I, \Phi'_P, \Phi'_I, \rho) - f_2(\mathbf{S}_P, \mathbf{S}_I, \Phi'_P, \Phi'_I, \rho) \geq t_0 \quad (3.68)$$

Furthermore, we can decompose the first posynomial as

$$f_1(\mathbf{S}_P, \mathbf{S}_I, \Phi'_P, \Phi'_I, \rho) = \sum_{k=1}^{K_1} g_{1k}(\mathbf{S}_P, \mathbf{S}_I, \Phi'_P, \Phi'_I, \rho) \quad (3.69)$$

With a proper choice of nonnegative $\{\gamma_{1k}\}$ satisfying $\sum_{k=1}^{K_1} \gamma_{1k} = 1$, (3.68) rewrites as

$$\frac{t_0 + f_2(\mathbf{S}_P, \mathbf{S}_I, \Phi'_P, \Phi'_I, \rho)}{f_1(\mathbf{S}_P, \mathbf{S}_I, \Phi'_P, \Phi'_I, \rho)} = (t_0 + f_2(\mathbf{S}_P, \mathbf{S}_I, \Phi'_P, \Phi'_I, \rho)) \prod_{k=1}^{K_1} \left(\frac{g_{1k}(\mathbf{S}_P, \mathbf{S}_I, \Phi'_P, \Phi'_I, \rho)}{\gamma_{1k}} \right)^{-\gamma_{1k}} \quad (3.70)$$

$$\leq 1 \quad (3.71)$$

Similarly, the denominator of rate constraint (3.13) is indeed a product of signomials, with each factor expressed as

$$1 + \frac{(1-\rho)}{\sigma_n^2} C_n = f_{1nk}(\mathbf{S}_P, \mathbf{S}_I, \mathbf{\Phi}'_P, \mathbf{\Phi}'_I, \rho) - f_{2nk}(\mathbf{S}_P, \mathbf{S}_I, \mathbf{\Phi}'_P, \mathbf{\Phi}'_I, \rho) \quad (3.72)$$

Therefore, we can rewrite the rate constraint (3.13) as

$$\prod_{n=0}^{N-1} \left(1 + \frac{(1-\rho)}{\sigma_n^2} C_n \right) = \prod_{n=0}^{N-1} (f_{1nk}(\mathbf{S}_P, \mathbf{S}_I, \mathbf{\Phi}'_P, \mathbf{\Phi}'_I, \rho) - f_{2nk}(\mathbf{S}_P, \mathbf{S}_I, \mathbf{\Phi}'_P, \mathbf{\Phi}'_I, \rho)) \quad (3.73)$$

$$\geq 2^{\bar{R}} \quad (3.74)$$

One possible approach is to unwrap the result of signomial multiplication as a new signomial. In this way, (3.74) is reduced to

$$f'_1(\mathbf{S}_P, \mathbf{S}_I, \mathbf{\Phi}'_P, \mathbf{\Phi}'_I, \rho) - f'_2(\mathbf{S}_P, \mathbf{S}_I, \mathbf{\Phi}'_P, \mathbf{\Phi}'_I, \rho) \geq 2^{\bar{R}} \quad (3.75)$$

which is equivalent to

$$\frac{2^{\bar{R}} + f'_2(\mathbf{S}_P, \mathbf{S}_I, \mathbf{\Phi}'_P, \mathbf{\Phi}'_I, \rho)}{f'_1(\mathbf{S}_P, \mathbf{S}_I, \mathbf{\Phi}'_P, \mathbf{\Phi}'_I, \rho)} \leq 1 \quad (3.76)$$

By decomposing $f'_1(\mathbf{S}_P, \mathbf{S}_I, \mathbf{\Phi}'_P, \mathbf{\Phi}'_I, \rho) = \sum_{j=1}^{J_1} g'_{1j}(\mathbf{S}_P, \mathbf{S}_I, \mathbf{\Phi}'_P, \mathbf{\Phi}'_I, \rho)$ and introducing another nonnegative coefficient set $\{\gamma'_{1j}\}$ with $\sum_{j=1}^{J_1} \gamma'_{1j} = 1$ for AM-GM inequality, it can be converted to

$$\left(2^{\bar{R}} + f'_2(\mathbf{S}_P, \mathbf{S}_I, \mathbf{\Phi}'_P, \mathbf{\Phi}'_I, \rho) \right) \prod_{j=1}^{J_1} \left(\frac{g'_{1j}(\mathbf{S}_P, \mathbf{S}_I, \mathbf{\Phi}'_P, \mathbf{\Phi}'_I, \rho)}{\gamma'_{1j}} \right)^{-\gamma'_{1j}} \leq 1 \quad (3.77)$$

Hence, the problem is transformed into a standard GP

$$\min_{\mathbf{S}_P, \mathbf{S}_I, \rho, \bar{\rho}, t_0} \quad 1/t_0 \quad (3.78)$$

$$\text{subject to} \quad \frac{1}{2} [\|\mathbf{S}_I\|_F^2 + \|\mathbf{S}_P\|_F^2] \leq P \quad (3.79)$$

$$(t_0 + f_2(\mathbf{S}_P, \mathbf{S}_I, \mathbf{\Phi}'_P, \mathbf{\Phi}'_I, \rho)) \prod_{k=1}^{K_1} \left(\frac{g_{1k}(\mathbf{S}_P, \mathbf{S}_I, \mathbf{\Phi}'_P, \mathbf{\Phi}'_I, \rho)}{\gamma_{1k}} \right)^{-\gamma_{1k}} \leq 1 \quad (3.80)$$

$$(2^{\bar{R}} + f'_2(\mathbf{S}_P, \mathbf{S}_I, \mathbf{\Phi}'_P, \mathbf{\Phi}'_I, \rho)) \prod_{j=1}^{J_1} \left(\frac{g'_{1j}(\mathbf{S}_P, \mathbf{S}_I, \mathbf{\Phi}'_P, \mathbf{\Phi}'_I, \rho)}{\gamma'_{1j}} \right)^{-\gamma'_{1j}} \leq 1 \quad (3.81)$$

$$\rho + \bar{\rho} \leq 1 \quad (3.82)$$

It is worth noting that the GP method is not the best optimization approach due to the predetermined suboptimal beamforming phases $\mathbf{\Phi}'_P, \mathbf{\Phi}'_I$. Also, the unwrap process from (3.73) to (3.75) significantly increases the computational complexity and is more suitable for small n and m . The procedure is concluded in Algorithm 5.

Algorithm 5 Waveform Design for Multiple Rectennas

- 1: **Initialize:** $i \leftarrow 0$, Φ'_P, Φ'_I in (3.66), $\mathbf{S}_P, \mathbf{S}_I$ in (3.67), $\rho, \bar{\rho} = 1 - \rho, \bar{R}, Z_{DC}^{(0)} = 0$
 - 2: **repeat**
 - 3: $i \leftarrow i + 1, \ddot{\mathbf{S}}_P \leftarrow \mathbf{S}_P, \ddot{\mathbf{S}}_I \leftarrow \mathbf{S}_I, \ddot{\rho} \leftarrow \rho, \ddot{\bar{\rho}} \leftarrow \bar{\rho}$
 - 4: $\gamma_{1k} \leftarrow g_{1k} \left(\ddot{\mathbf{S}}_P, \ddot{\mathbf{S}}_I, \Phi'_P, \Phi'_I, \ddot{\rho} \right) / f_1 \left(\ddot{\mathbf{S}}_P, \ddot{\mathbf{S}}_I, \Phi'_P, \Phi'_I, \ddot{\rho} \right), k = 1, \dots, K_1$
 - 5: $\gamma'_{1j} \leftarrow g'_{1j} \left(\ddot{\mathbf{S}}_P, \ddot{\mathbf{S}}_I, \Phi'_P, \Phi'_I, \ddot{\rho} \right) / f'_1 \left(\ddot{\mathbf{S}}_P, \ddot{\mathbf{S}}_I, \Phi'_P, \Phi'_I, \ddot{\rho} \right), j = 1, \dots, J_1$
 - 6: $\mathbf{S}_P, \mathbf{S}_I, \rho, \bar{\rho} \leftarrow \arg \min (3.78) - (3.82)$
 - 7: $Z_{DC}^{(i)} \leftarrow Z_{DC}(\mathbf{S}_P, \mathbf{S}_I, \Phi'_P, \Phi'_I, \rho)$
 - 8: **until** $\left| Z_{DC}^{(i)} - Z_{DC}^{(i-1)} \right| < \epsilon$ or $i = i_{\max}$
-

Chapter 4

Performance Evaluation

In this section, we simulate the target systems with MATLAB and perform the optimizations using CVX. We also characterize and compare the R-E regions based on different configurations. The multipath channel is implemented with Hiper-LAN/2 model B [39], where the 18 taps are modeled as i.i.d. CSCG variables with normalized average power. Table 4.1 summarizes the reference parameters in the simulation. In the following sections, the settings will be employed unless otherwise stated.

Table 4.1: Reference parameters used in the simulation

	Parameter	Value
Transceiver	Truncation order	$n_o = 4$
	Diode k-parameters	$k_2 = 0.0034; k_4 = 0.3829$
	Antenna resistance	$R_{\text{ant}} = 50 \Omega$
	Transmit antenna	$M = 1$
	Receive antenna	$U = 1$
	Average transmit power	$P_{\text{rf}}^t = -20 \text{ dBm}$
	Average receive power	$P_{\text{rf}}^r = -20 \text{ dBm}$
	Average Noise power	$\sigma_n^2 = -40 \text{ dBm}$
	Effective isotropic radiated power	$\text{EIRP} = 36 \text{ dBm}$
	Receive antenna gain	$G_r = 2 \text{ dBi}$
Channel	Minimum current gain per iteration	$\varepsilon = 0.05 \mu\text{A}$
	Center frequency	$f_0 = 5.18 \text{ GHz}$
	Path loss	$PL = 58 \text{ dB}$
	Tap	$L = 18$
	Bandwidth	$B = 1 \text{ MHz}$
	Subband	$N = 16$
	Frequency gap	$\Delta f = 62.5 \text{ kHz}$
	SNR	$\text{SNR} = 20 \text{ dB}$

4.1 SISO

Fig. 4.1 illustrates the frequency response of a SISO FF and FS channel based on the same tap delays and tap gains.

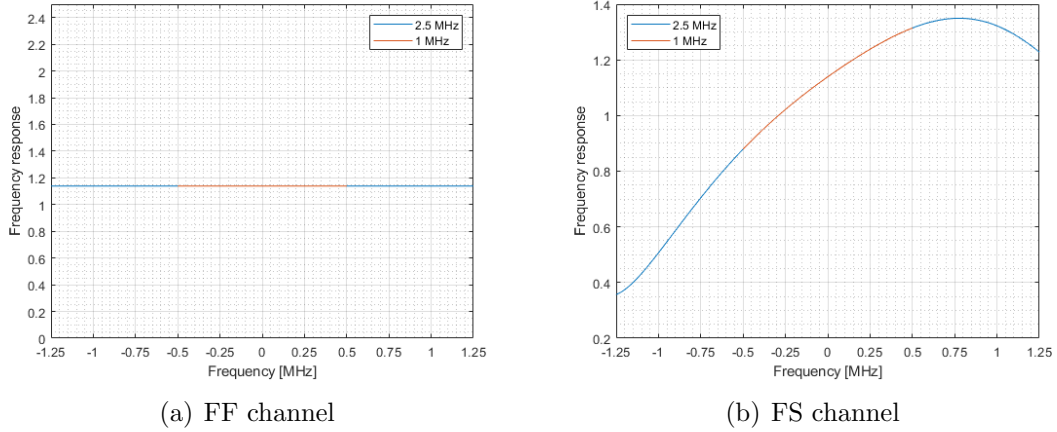


Figure 4.1: Frequency response of the SISO FF and FS channels

In the R-E plots, the rightmost point of each curve indicates the maximum achievable rate with zero harvested DC current. It corresponds to WIT that allocates all available power to the modulated information waveform by the water-filling algorithm with $\rho = 0$. Note that the x-axis here refers to the per-subband rate and is normalized w.r.t. bandwidth. With a fixed power budget, the power received by each subband decreases as N increases. Therefore, the rate achieved by each subband decreases but the total rate increases. On the other hand, the leftmost point corresponds to the maximum output DC current with zero information rate, which correspond to allocating all power to the multisine waveform with $\rho = 1$ (WPT).

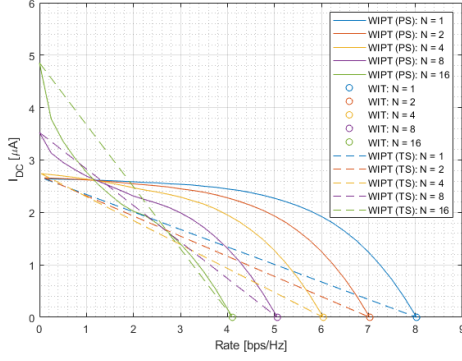
Nevertheless, the discrete rate constraint (3.9) in the optimization problem prevent the solutions from achieving the absolute WIT points using the proposed WIPT approach. Therefore, we perform an individual WIT and combine the results for closed R-E plots.

4.1.1 R-E Region vs Subband

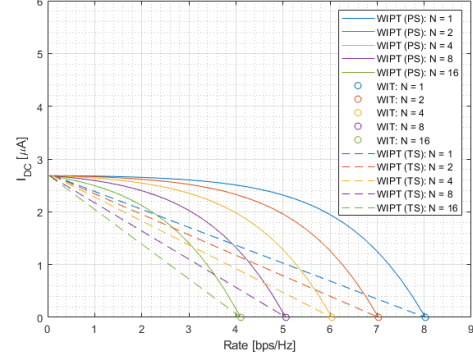
Fig. 4.2 illustrates the R-E region against subband $N = 1, 2, 4, 8, 16$ for superposed waveform and no power waveform over FF and FS channels respectively.

It can be observed that the introduction of multisine power waveform boosts the harvested energy for $N > 4$ where the superposed waveform outperforms the modulated signal for WIPT. In contrast, the R-E performance of both signals are very close for $N \leq 4$ so that multisine is unnecessary. The reason is that the fourth order terms of power and information waveforms (2.42) and (2.48) have different contribution to the harvested DC current. Despite both posynomials consist of monomials of similar magnitude ($\prod_{j=0}^3 s_{P,n_j,m_j} A_{n_j,m_j}$ and $\prod_{j=0,2} s_{I,n_0,m_j} A_{n_0,m_j} \prod_{j=1,3} s_{I,n_1,m_j} A_{n_1,m_j}$), the power posynomial contains $(2N^3 + N)/3$ monomials but the information posynomial only holds N^2 monomials. Therefore, the energy benefit of multisine is amplified with a large N . Although it seems that a very large N can significantly increases the output DC current, this is not true because each subband will receive less power such that the amplitude of monomials decreases accordingly.

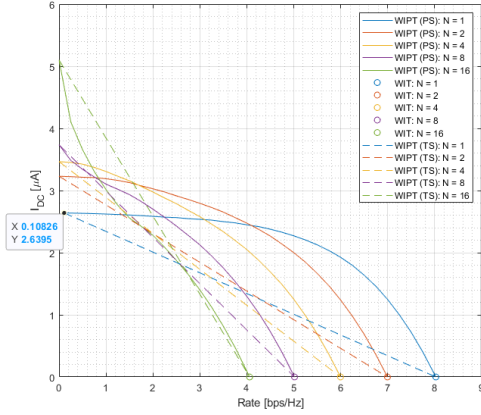
A contrast of R-E plots on FF and FS channels also indicates the benefit of frequency selectivity on the harvested power. The gain is particularly obvious in the low-rate region, where all the power is allocated to the subband with the strongest



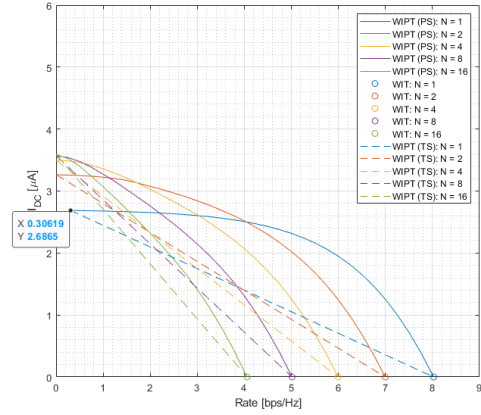
(a) FF: Superposed waveform



(b) FF: No power waveform



(c) FS: Superposed waveform



(d) FS: No power waveform

Figure 4.2: R-E region vs N for FF and FS channels

amplitude. We observe from the FS channel instance in Fig. 4.1(b) that some edge frequencies enjoy a larger gain than the center frequency, whose advantage is exploited when more subbands are used. In comparison, the small amplitude at the center frequency accounts for the lower output DC current when $N = 1$ (indicated by the blue curves in Fig. 4.2(c) and 4.2(d)).

Without power waveform, the R-E region appears convex such that PS dominates TS over all N . On the other hand, the R-E region achieved by superposed waveform with PS is convex for $N = 2, 4$ but concave-convex for $N = 8, 16$. Therefore, the optimal strategy is using PS for small N , TS for large N , and a combination of PS and TS for medium N . As shown in Fig. 4.3, the best curve for medium N consists of two parts. The straight part is achieved by TS between WPT (multisine only with $\rho = 1$) that corresponds to the leftmost point and WIPT (superposed waveform with $0 < \rho < 1$) that corresponds to the tangent point, while the convex part is the contribution of WIPT only. The characteristics of the optimal R-E region comes from the rectifier nonlinearity.

Moreover, the plots over the FS channel suggests that for single-carrier transmission, the modulated waveform outperforms the superposed waveform for WPT. At a zero-approaching rate, the modulated waveform produces a DC current of $2.69 \mu\text{A}$ while the superposed waveform only delivers $2.64 \mu\text{A}$. The actual current

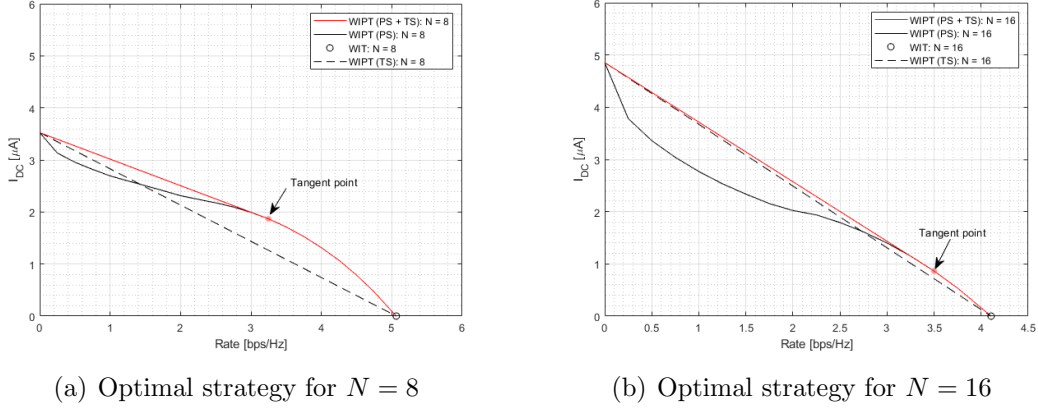


Figure 4.3: Optimal R-E region for FF channel with medium N

gap is even larger since the former still guarantees a slightly higher rate. On the contrary, the superposed waveform leads to a larger harvested current for $N \geq 2$. It demonstrates that modulation is beneficial in single-carrier transmission but can be detrimental in multi-carrier transmission. The reason is that the modulation gain (2.45) of modulated waveform outperforms the energy benefit of multisine in single-carrier transmission but is outperformed in multi-carrier transmission. The result is inline with the scaling laws proposed in [11].

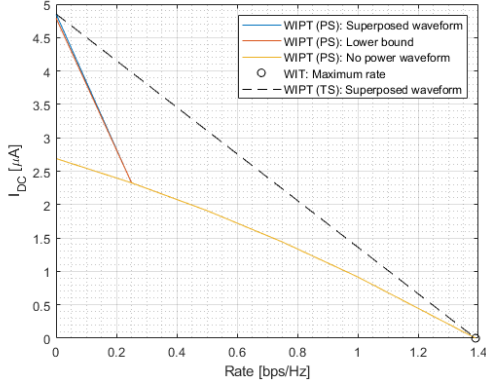
One problem is that the leftmost point of some curves did not start from the y-axis. Although a zero rate constraint is employed in WIPT, a candidate solution may achieve a nonzero rate. It is because the current gain of the next iteration is smaller than the threshold ε so that the algorithm terminates and outputs the existing R-E pair. This phenomenon occurs primarily for small N that produces a smaller current gain in each iteration and at the low-rate region where the output DC current almost saturated. It can be fixed either by reducing the threshold ε or developing an individual function for WPT.

4.1.2 R-E Region vs SNR

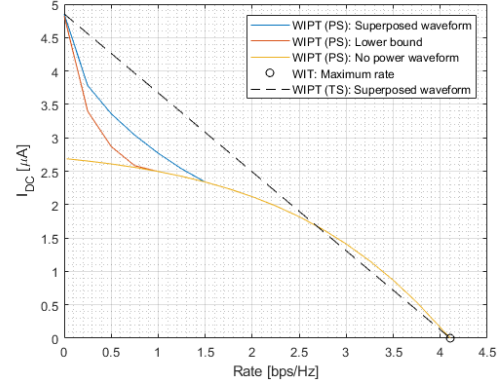
Fig. 4.4 and 4.5 contrast the performance of the modulated waveform, ideal superposed waveform and its lower bound for $N = 16$ and SNR = 10, 20, 30, 40 dB over the example FF and FS channels.

Thanks to the contribution of multisine waveform, the R-E region of the superposed signal is enlarged in both cases. This phenomenon is especially obvious in the low-rate region, where the multisine dominates the transmission. It results from the fact that the nonlinear rectifier favors the deterministic multisine with high PAPR. On the contrary, there is some randomness involved in the modulated waveform that produces fluctuations to the rectifier and leads to some power loss [11]. This phenomenon is in sharp contrast to the conclusion based on linear harvester model that both waveforms are equally suitable for WPT [40]. As shown in the plots, even with the assumption that the deterministic power waveform creates some interference to the information waveform, the rate loss is compensated by the power gain such that the superposed waveform strictly outperforms the modulated waveform.

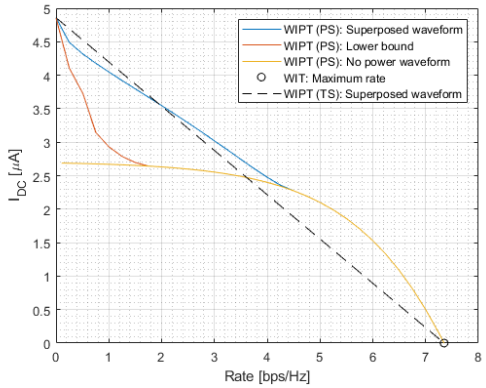
Another observation is the performance gap between the ideal superposed wave-



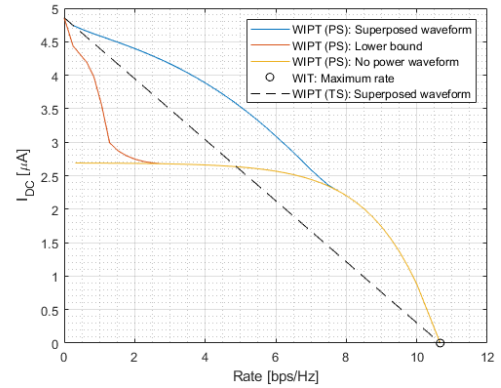
(a) FF: SNR = 10 dB



(b) FF: SNR = 20 dB



(c) FF: SNR = 30 dB



(d) FF: SNR = 40 dB

Figure 4.4: R-E region vs SNR for FF channel

form and its lower bound widens as SNR increases. This is as expected because the rate is dominated by noise at low SNR and by interference at high SNR. For SNR = 10 dB, the interference is much lower than noise even if a large amount of power is allocated to the multisine component. Hence, the curves almost overlap with each other. On the other hand, at a higher SNR, the rate loss by interference increases while the energy benefit of power waveform remains unchanged. To obtain the optimal R-E tradeoff, the transmitter tends to allocate less power to the multisine so that the harvested current drops. Therefore, the rate boost of deterministic power waveform grows as SNR increases.

The plots also demonstrate that for the superposed waveform with a sufficiently large N , TS is preferred at low SNR and PS is favored at high SNR, while a combination of TS and PS is generally optimal for medium SNR. On the other hand, the R-E region is strictly convex for the modulated waveform-only transmission due to its inefficiency to boost the harvested energy. It corresponds to the conventional opinion that PS always outperforms TS for no power waveform transmission. In this case, the R-E curve is approximately straight at low SNR but with large curvature at high SNR. The reason is that at a low SNR, the water-filling strategy concentrates the power to the best subband to maximize the rate, and the region boundary is obtained by varying ρ only. In comparison, more subbands are utilized in the transmission as SNR increases. Therefore, only a small portion of power is

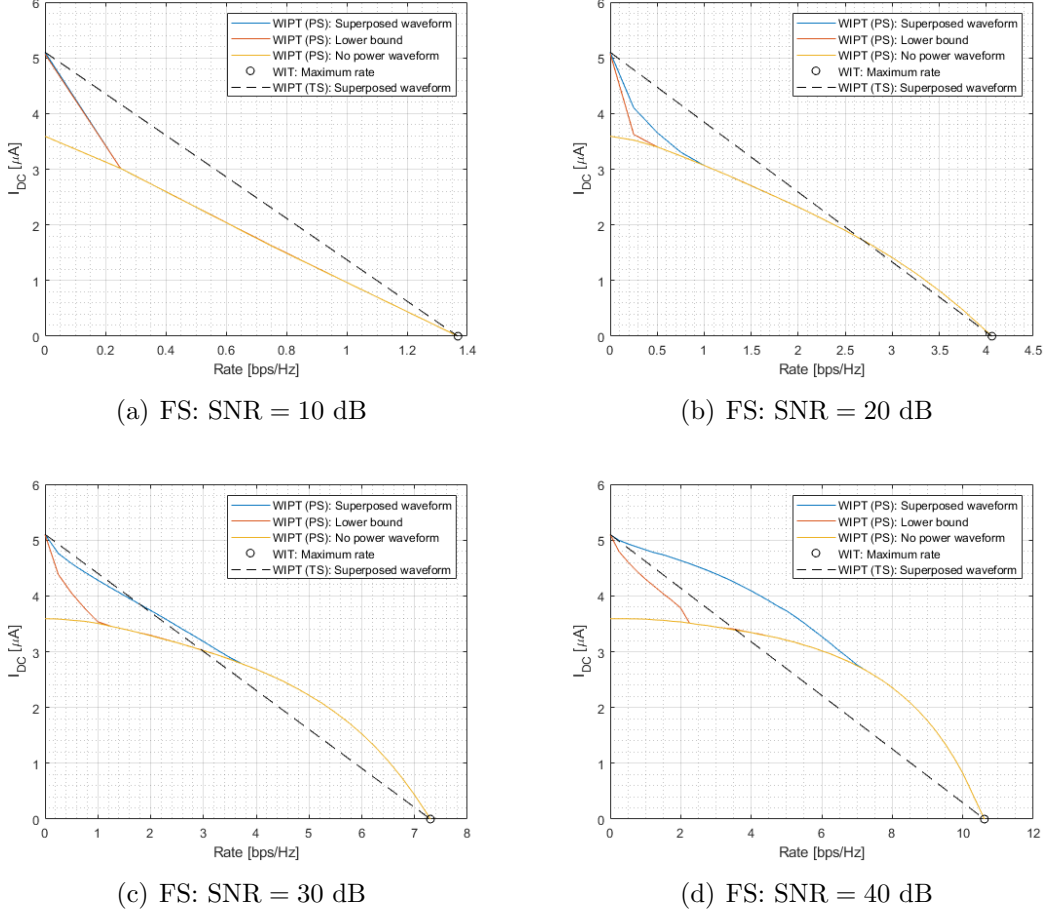


Figure 4.5: R-E region vs SNR for FS channel

required to achieve a decent rate while the remaining part can be used to boost the output current.

A comparison between the results over FF and FS channels emphasizes the benefit of frequency selectivity on the harvested current. The gain is more significant for modulated waveform (around $1 \mu A$) than superposed waveform (around $0.25 \mu A$). One possible reason is that the power are concentrated in few subbands such that the number of terms in (2.42) and (2.48) are comparable. In such cases, the impact of channel amplitude on each monomial is more significant on the information waveform and contributes to a larger gain in the harvested current.

4.1.3 R-E Region vs PAPR

Fig. 4.6 investigates the relationship between PAPR and R-E region for $N = 8, 16$ over the FF and FS channels.

A first observation is that a large enough PAPR is required to fully exploit the power gain of the multisine waveform. For $N = 16$, the R-E region is convex for a PAPR no larger than 20 dB and is concave-convex when it increases to 30 dB. For instance, with a small PAPR of 10 dB, the use of multisine waveform is strictly constrained such that the modulated waveform dominates the transmit signal. Hence, the corresponding R-E plot is similar to the result without power

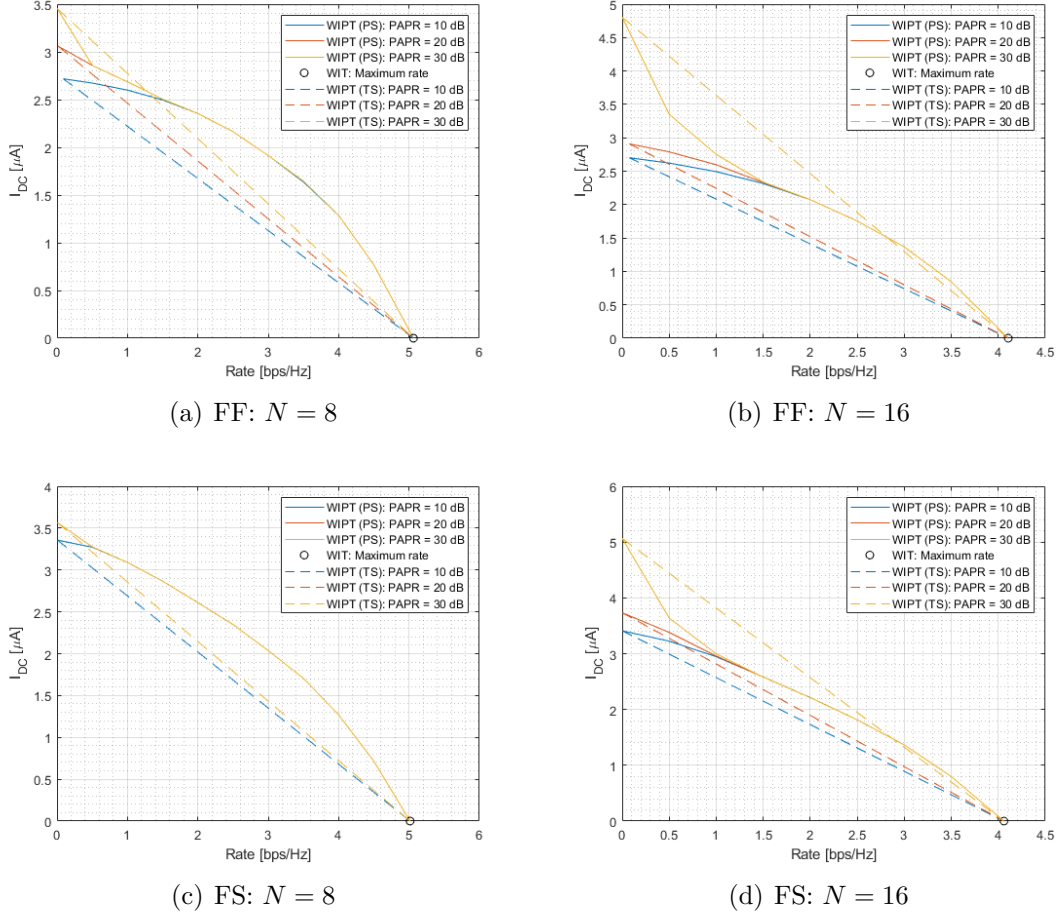


Figure 4.6: R-E region vs PAPR for FF channel

waveform. On the contrary, a PAPR of 30 dB is large enough to achieve the optimal performance of the superposed signal in the low-rate region. It can be concluded that the energy benefit of the multisine waveform indeed comes from the high PAPR. In each cycle, the peak pushes the rectifier output voltage to a high level which decreases slowly in the rest of the period.

A contrast of the R-E plots of $N = 8$ and 16 also suggests a larger N requires higher PAPR to improve the performance. When PAPR increases from 20 to 30 dB, the current gain is more significant for $N = 16$ than $N = 8$. On the other hand, the impact of PAPR for small N is not as significant as for large N . This verifies the positive correlation between N and PAPR discussed in Section 2.2.1. Although increasing N in a proper range can effectively boost the harvested energy, the PAPR constraint may limit the use of a large N in practice.

It is interesting to notice that the frequency selectivity helps to achieve the optimal R-E region with a lower PAPR. As shown in Fig. 4.6(c), a PAPR constraint of 20 dB is enough to guarantee the best tradeoff and a larger budget is unnecessary. However, the transmission over the FF channel requires a larger PAPR of 30 dB to achieve optimum behavior. This is because frequency selective channel can further amplify the difference of frequency components such that the received signal is with enhanced PAPR.

The main disadvantage of the proposed approach is that the oversampling pro-

cedure further increases the overall computational complexity in the optimization.

4.2 MISO

Next, we focus on the MISO case and investigate the influence of transmit antenna M and subband N on the R-E performance over typical multipath FF and FS channels. Thanks to the decoupling approach, the predetermined beamforming phases Φ_I^* , Φ_P^* are optimal for MISO and the computational complexity is irrelevant to M . Fig. 4.7 shows the frequency response employed in the optimization for $M = 2$ and 3.

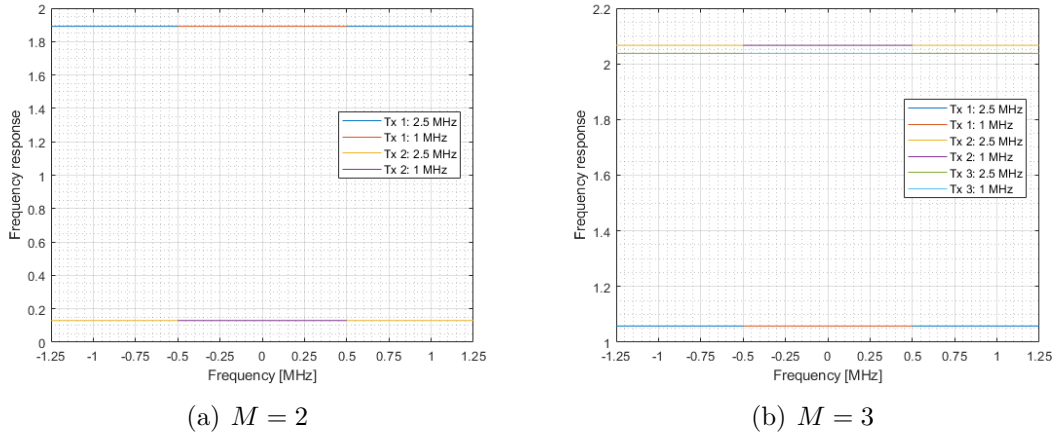


Figure 4.7: Frequency response of the MISO FF channels

The corresponding R-E regions for $N = 4$ and 8 are illustrated in Fig. 4.8.

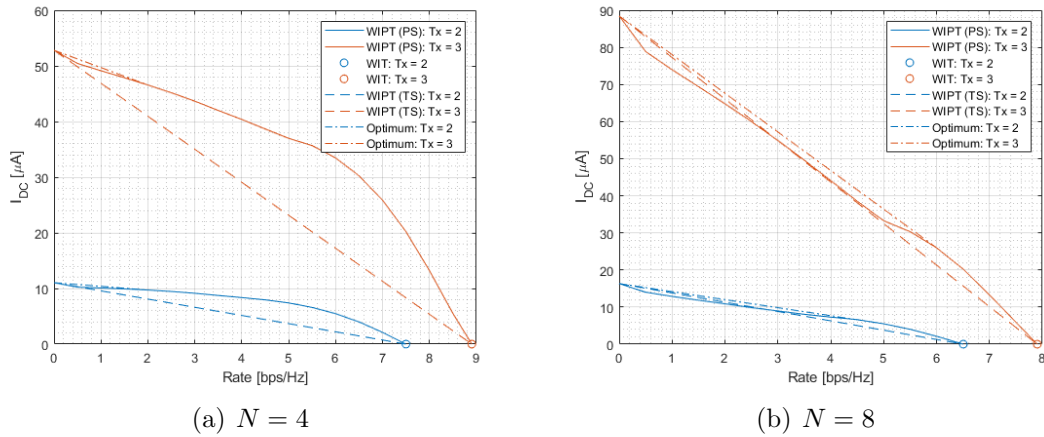


Figure 4.8: R-E region vs M and N over typical FF channels

A first observation is that the concavity-convexity start to appear from $N = 4$ for the MISO systems, in contrast to $N = 8$ in the previous SISO case. The trend becomes more obvious as N increases. The plots also suggest that a large M can significantly boost the energy benefit of the multisine waveform. In this particular instance, raising M from 2 to 3 produce a current gain of around 400 %. Although

this value partially results from the difference in channel amplitude, it highlights the benefit of using multiple antennas in WIPT. The reason is that increasing M essentially enhances the subchannels such that the terms contributing to the harvested current are amplified. Also, a smaller N is needed to achieve a certain output current level, which further reduces the signal PAPR. Hence, increasing M can be a possible solution for PAPR-constrained systems. Moreover, a combination of TS (between WPT and WIPT) at a low rate and PS at high rate guarantees the optimal R-E region as a convex hull.

To eliminate the influence of channel randomness, we investigate the rate and energy performance for 100 FF channels with $N = 4$. Fig. 4.9 shows the Cumulative Distribution Function (CDF) of maximum rate and current that correspond to WIT and WPT respectively. It is less interesting for WIPT since the variation trend of the R-E tradeoff is not presented. A better representation is required to avoid channel randomness and characterize the general R-E region.

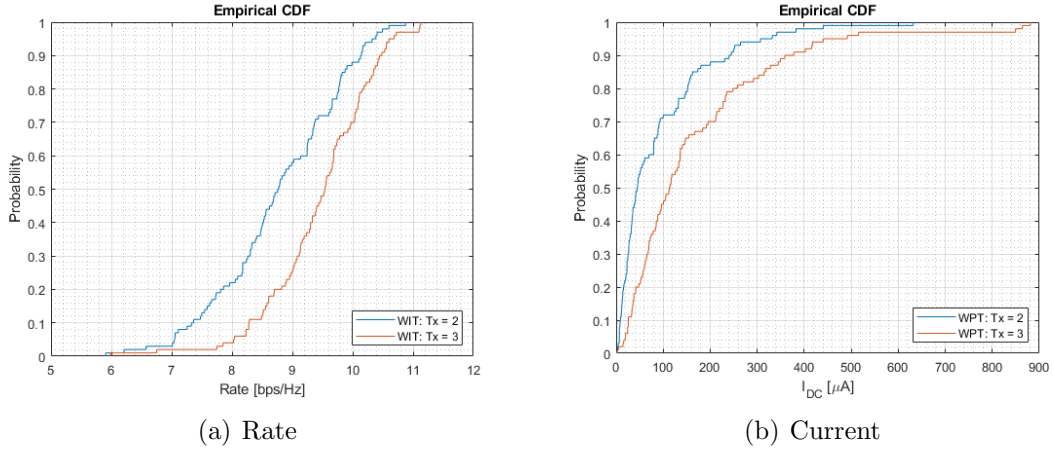


Figure 4.9: Rate and current CDF vs M for MISO FF channels

4.3 MIMO

We then explore the impact of receive antenna U and subband N on the R-E region for MIMO systems with transmit antenna $M = 2$ over a typical FF channel. The dominant eigenvalue of each subband is shown in Fig. 4.10.

As illustrated in Fig. 4.11, a contrast between $U = 2$ and 3 suggests that increasing U may boost the rate and energy simultaneously, thanks to the multiplexing gain of MIMO. For a fixed $M = 2$, increasing U from 2 to 3 provides no extra streams for transmission but produces a larger channel eigenvalue, which benefits the R-E region by increasing the effective subband amplitude.

On the other hand, a large N amplifies the harvested power as expected from the rectifier nonlinearity. It can be observed that the R-E curves begin to show some concavity-convexity for $N = 4$, which was first observed for $N = 8$ in SISO channels. A possible reason is that each subchannel in this case has 2 virtual streams so that the equivalent subband is indeed $4 \times 2 = 8$. Therefore, MIMO demonstrates a twofold benefit in rate and energy. It requires a smaller N to achieve a certain output power level and is more suitable for PAPR-constrained devices.

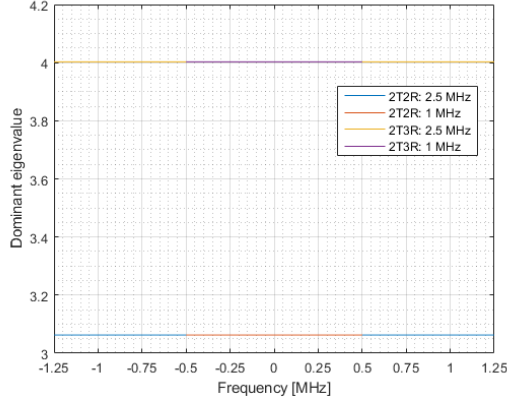


Figure 4.10: Frequency response of the MIMO FF channel

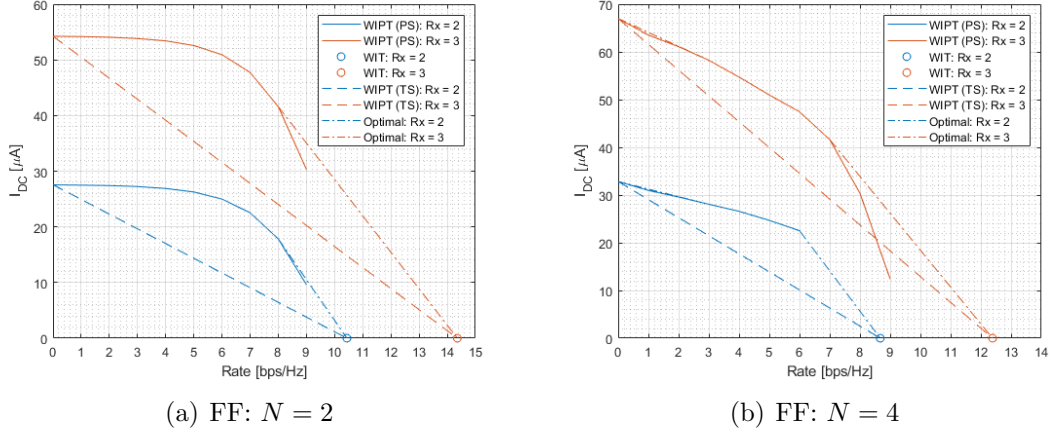


Figure 4.11: R-E region vs N and U for MIMO FF channels

The main problem of the plot is that the rightmost points of the R-E curves do not reach the x-axis. It results from the discrete rate constraints employed in the simulation. With a step of 1 bps/Hz, the points tend to locate near the integer rates. For instance, the plot corresponding to $U = 2$ and $N = 4$ terminates at a rate of 6 bps/Hz with an output current of 22 μA , indicating the proposed PS-WIPT strategy cannot achieve the next rate milestone of 7 bps/Hz. The reason is that the suboptimal phases Φ'_P, Φ'_I are determined before the optimization so that the algorithm cannot reach the channel capacity corresponding to WIT. Therefore, the proposed GP approach is suboptimal for MIMO systems.

For a fixed M and U , a good R-E tradeoff can be obtained by a combination of the following strategies. In the low-rate region, we can use PS-WIPT for a small N and employ TS between WPT and WIPT for a large N . In the medium-rate region, PS-WIPT can generally guarantee a decent tradeoff between rate and energy. When the rate constraint is high, TS between WIT and WIPT is the best strategy to enjoy the benefit of multisine and avoid the rate loss of suboptimal phases.

Despite as expected, the conclusions require more evidence since only one specific channel is investigated in the simulation.

Chapter 5

Conclusions and Future Works

This paper performed waveform optimization and rate-energy region characterization for a point-to-point WIPT. Based on the diode nonlinear model, a superposition of multi-carrier modulated and unmodulated waveforms at the transmitter are jointly optimized with the power splitter at the receiver. The signal design is modeled as a non-convex posynomial maximization problem adaptive to the CSI. We also extend the existing work to MIMO systems and consider the PAPR constraints.

Numerical results demonstrate the following conclusions. First, the harvester nonlinearity can be exploited to boost the harvested energy. It prefers a different waveform design, transceiver architecture, and resource allocation. Second, modulation benefits the delivered power in single-carrier transmission but is detrimental for multi-carrier WIPT. Third, the superposed signal can effectively enlarge the R-E region with the twofold benefit of multisine. Fourth, a combination of PS and TS is generally the optimal receiver strategy. Fifth, frequency selectivity has a positive influence on the harvested energy. Sixth, increasing Tx and/or Rx not only improves the rate-energy tradeoff but also reduces the PAPR requirement.

Some limitations of this work require further attention. First, the adaptive design relies on perfect CSIT and synchronization between transmitter and receiver, but both conditions can be hard to achieve. Second, the power splitting ratio can be difficult to adjust dynamically in practice. Third, the GP approach is suboptimal for MIMO systems. Fourth, the iterative algorithms are sensitive to initialization and time-consuming when a large number of subbands and/or antennas are employed.

Several novel ideas in recent research may be further integrated with this paper. For instance, the optimal approach for MIMO WIPT is discussed in [41]. Also, [42] proposed a dual-mode SWIPT with an adaptive *Mode Switching* (MS) algorithm to alternate between single-tone and multi-tone transmission. The former employs a multi-energy level signaling with PSK for high rate communication, while the latter modulates the multisine waveform by PAPR for power-demanding applications [43]. A generic receiver architecture for MIMO WPT was designed in [44], which demonstrated that using multiple rectifiers with proper beamforming and power allocation scheme can significantly improve the harvested power. Moreover, another nonlinear EH model was proposed in [14] whose parameters relies on a logistic curve fitting technique.

Appendix A

Appendix

The source code and relevant materials can be retrieved from [\[this link\]](#).

Bibliography

- [1] B. Clerckx, A. Costanzo, A. Georgiadis, and N. Borges Carvalho, “Toward 1G Mobile Power Networks: RF, Signal, and System Designs to Make Smart Objects Autonomous,” *IEEE Microwave Magazine*, vol. 19, no. 6, pp. 69–82, 2018.
- [2] M. S. Trotter, J. D. Griffin, and G. D. Durgin, “Power-optimized waveforms for improving the range and reliability of RFID systems,” *2009 IEEE International Conference on RFID, RFID 2009*, pp. 80–87, 2009.
- [3] B. Clerckx and E. Bayguzina, “Waveform Design for Wireless Power Transfer,” *IEEE Transactions on Signal Processing*, vol. 64, no. 23, pp. 6313–6328, 2016.
- [4] B. Clerckx, R. Zhang, R. Schober, D. W. K. Ng, D. I. Kim, and H. V. Poor, “Fundamentals of wireless information and power transfer: From RF energy harvester models to signal and system designs,” *IEEE Journal on Selected Areas in Communications*, vol. 37, no. 1, pp. 4–33, 2019.
- [5] D. W. K. Ng, T. Q. Duong, C. Zhong, and R. Schober, *Wireless Information and Power Transfer: Theory and Practice*. Wiley-IEEE Press, 2019.
- [6] L. R. Varshney, “Transporting Information and Energy Simultaneously,” *IEEE International Symposium on Information Theory - Proceedings*, pp. 1612–1616, 2008.
- [7] P. Grover and A. Sahai, “Shannon meets tesla: Wireless information and power transfer,” *IEEE International Symposium on Information Theory - Proceedings*, pp. 2363–2367, 2010.
- [8] R. Zhang and C. K. Ho, “MIMO broadcasting for simultaneous wireless information and power transfer,” *IEEE Transactions on Wireless Communications*, vol. 12, no. 5, pp. 1989–2001, 2013.
- [9] X. Zhou, R. Zhang, and C. K. Ho, “Wireless information and power transfer in multiuser OFDM systems,” *GLOBECOM - IEEE Global Telecommunications Conference*, vol. 13, no. 4, pp. 4092–4097, 2013.
- [10] L. Liu, R. Zhang, and K. C. Chua, “Wireless information and power transfer: A dynamic power splitting approach,” *IEEE Transactions on Communications*, vol. 61, no. 9, pp. 3990–4001, 2013.
- [11] B. Clerckx, “Wireless Information and Power Transfer: Nonlinearity, Waveform Design, and Rate-Energy Tradeoff,” *IEEE Transactions on Signal Processing*, vol. 66, no. 4, pp. 847–862, 2018.

- [12] M. Varasteh, E. Piovano, and B. Clerckx, "A Learning Approach To Wireless Information and Power Transfer Signal and System Design," pp. 4534–4538, 2018. [Online]. Available: <http://arxiv.org/abs/1810.12152>
- [13] S. Y. Hui, W. Zhong, and C. K. Lee, "A critical review of recent progress in mid-range wireless power transfer," *IEEE Transactions on Power Electronics*, vol. 29, no. 9, pp. 4500–4511, 2014.
- [14] E. Boshkovska, D. W. K. Ng, N. Zlatanov, and R. Schober, "Practical non-linear energy harvesting model and resource allocation for SWIPT systems," *IEEE Communications Letters*, vol. 19, no. 12, pp. 2082–2085, 2015.
- [15] Y. Zeng, B. Clerckx, and R. Zhang, "Communications and Signals Design for Wireless Power Transmission," *IEEE Transactions on Communications*, vol. 65, no. 5, pp. 2264–2290, 2017.
- [16] A. S. Boaventura and N. B. Carvalho, "Maximizing DC power in energy harvesting circuits using multisine excitation," *IEEE MTT-S International Microwave Symposium Digest*, vol. 1, no. 1, pp. 1–4, 2011.
- [17] T. Takahashi, T. Mizuno, M. Sawa, T. Sasaki, T. Takahashi, and N. Shinohara, "Development of phased array for high accurate microwave power transmission," *2011 IEEE MTT-S International Microwave Workshop Series on Innovative Wireless Power Transmission: Technologies, Systems, and Applications, IMWS-IWPT 2011 - Proceedings*, pp. 157–160, 2011.
- [18] Y. S. Chen and C. W. Chiu, "Maximum achievable power conversion efficiency obtained through an optimized rectenna structure for RF energy harvesting," *IEEE Transactions on Antennas and Propagation*, vol. 65, no. 5, pp. 2305–2317, 2017.
- [19] A. Collado and A. Georgiadis, "Optimal waveforms for efficient wireless power transmission," *IEEE Microwave and Wireless Components Letters*, vol. 24, no. 5, pp. 354–356, 2014.
- [20] A. Boaventura, D. Belo, R. Fernandes, A. Collado, A. Georgiadis, and N. B. Carvalho, "Boosting the Efficiency: Unconventional Waveform Design for Efficient Wireless Power Transfer," *IEEE Microwave Magazine*, vol. 16, no. 3, pp. 87–96, 2015.
- [21] A. Dolgov, R. Zane, and Z. Popovic, "Power management system for online low power RF energy harvesting optimization," *IEEE Transactions on Circuits and Systems I: Regular Papers*, vol. 57, no. 7, pp. 1802–1811, 2010.
- [22] J. A. G. Akkermans, M. C. Van Beurden, G. J. N. Doodeman, and H. J. Visser, "Analytical models for low-power rectenna design," *IEEE Antennas and Wireless Propagation Letters*, vol. 4, no. 1, pp. 187–190, 2005.
- [23] A. Boaventura, A. Collado, N. B. Carvalho, and A. Georgiadis, "Optimum behavior: Wireless power transmission system design through behavioral models and efficient synthesis techniques," *IEEE Microwave Magazine*, vol. 14, no. 2, pp. 26–35, 2013.

- [24] M. Stoopman, S. Keyrouz, H. J. Visser, K. Philips, and W. A. Serdijn, "Co-design of a CMOS rectifier and small loop antenna for highly sensitive RF energy harvesters," *IEEE Journal of Solid-State Circuits*, vol. 49, no. 3, pp. 622–634, 2014.
- [25] C. R. Valenta and G. D. Durgin, "Harvesting wireless power: Survey of energy-harvester conversion efficiency in far-field, wireless power transfer systems," *IEEE Microwave Magazine*, vol. 15, no. 4, pp. 108–120, 2014.
- [26] A. Georgiadis, A. Collado, S. Via, and C. Meneses, "Flexible hybrid solar/EM energy harvester for autonomous sensors," *IEEE MTT-S International Microwave Symposium Digest*, pp. 1–4, 2011.
- [27] A. Collado and A. Georgiadis, "Conformal hybrid solar and electromagnetic (EM) energy harvesting rectenna," *IEEE Transactions on Circuits and Systems I: Regular Papers*, vol. 60, no. 8, pp. 2225–2234, 2013.
- [28] J. O. McSpadden, L. Fan, and K. Chang, "Design and Experiments of a High-Conversion-Efficiency 5.8-GHz Rectenna," *IEEE Transactions on Microwave Theory and Techniques*, vol. 46, no. 12, pp. 2053–2060, 1998.
- [29] J. Guo and X. Zhu, "An improved analytical model for RF-DC conversion efficiency in microwave rectifiers," *IEEE MTT-S International Microwave Symposium Digest*, pp. 1–3, 2012.
- [30] A. Costanzo and D. Masotti, "Smart Solutions in Smart Spaces: Getting the Most from Far-Field Wireless Power Transfer," *IEEE Microwave Magazine*, vol. 17, no. 5, pp. 30–45, 2016.
- [31] H. Sun, Z. Zhong, and Y. X. Guo, "An adaptive reconfigurable rectifier for wireless power transmission," *IEEE Microwave and Wireless Components Letters*, vol. 23, no. 9, pp. 492–494, 2013.
- [32] B. Strassner and K. Chang, "Microwave power transmission: Historical milestones and system components," *Proceedings of the IEEE*, vol. 101, no. 6, pp. 1379–1396, 2013.
- [33] B. Clerckx and E. Bayguzina, "Low-Complexity Adaptive Multisine Waveform Design for Wireless Power Transfer," *IEEE Antennas and Wireless Propagation Letters*, vol. 16, no. 1, pp. 2207–2210, 2017.
- [34] J.-p. Curty, N. Joehl, C. Dehollain, and M. J. Declercq, "A Model for Mu-Power Rectifier Analysis and Design," *Technology*, vol. 52, no. 12, pp. 2771–2779, 2005. [Online]. Available: [#](http://scholar.google.com/scholar?hl=en&btnG=Search&q=intitle:A+Model+for+-Power+Rectifier+Analysis+and+Design)0
- [35] M. Varasteh, B. Rassouli, and B. Clerckx, "On Capacity-Achieving Distributions for Complex AWGN Channels Under Nonlinear Power Constraints and their Applications to SWIPT," vol. 2017, 2017. [Online]. Available: <http://arxiv.org/abs/1712.01226>

- [36] S. Boyd, S. J. Kim, L. Vandenberghe, and A. Hassibi, “A tutorial on geometric programming,” *Optimization and Engineering*, vol. 8, no. 1, pp. 67–127, 2007.
- [37] M. Chiang, *Geometric Programming for communication systems*, 2005, vol. 2, no. 1-2.
- [38] B. R. Marks and G. P. Wright, “Technical Note—A General Inner Approximation Algorithm for Nonconvex Mathematical Programs,” *Operations Research*, vol. 26, no. 4, pp. 681–683, 1978.
- [39] J. Medbo and P. Schramm, “Channel Models for Hiperlan/2 in Different Indoor Scenarios,” *ETSI EP BRAN*, vol. 3ERI085B, 1998.
- [40] J. Xu, L. Liu, and R. Zhang, “Multiuser miso beamforming for simultaneous wireless information and power transfer,” *IEEE Transactions on Signal Processing*, vol. 62, no. 18, pp. 4798–4810, 2014.
- [41] Y. Huang and B. Clerckx, “Large-Scale Multiantenna Multisine Wireless Power Transfer,” *IEEE Transactions on Signal Processing*, vol. 65, no. 21, pp. 5812–5827, nov 2017. [Online]. Available: <http://ieeexplore.ieee.org/document/8008785/>
- [42] J. J. Park, J. H. Moon, K. Y. Lee, and D. I. Kim, “Dual Mode SWIPT: Waveform Design and Transceiver Architecture with Adaptive Mode Switching Policy,” *IEEE Vehicular Technology Conference*, vol. 2018-June, pp. 1–5, 2018.
- [43] I. Krikidis and C. Psomas, “Tone-index Multisine Modulation for SWIPT,” *arXiv preprint*, pp. 1–5, jun 2019. [Online]. Available: <http://arxiv.org/abs/1906.10386>
- [44] G. Ma, J. Xu, Y. Zeng, and M. R. V. Moghadam, “A Generic Receiver Architecture for MIMO Wireless Power Transfer with Nonlinear Energy Harvesting,” *IEEE Signal Processing Letters*, vol. 26, no. 2, pp. 312–316, 2019.